



저작자표시-비영리-변경금지 2.0 대한민국

이용자는 아래의 조건을 따르는 경우에 한하여 자유롭게

- 이 저작물을 복제, 배포, 전송, 전시, 공연 및 방송할 수 있습니다.

다음과 같은 조건을 따라야 합니다:



저작자표시. 귀하는 원저작자를 표시하여야 합니다.



비영리. 귀하는 이 저작물을 영리 목적으로 이용할 수 없습니다.



변경금지. 귀하는 이 저작물을 개작, 변형 또는 가공할 수 없습니다.

- 귀하는, 이 저작물의 재이용이나 배포의 경우, 이 저작물에 적용된 이용허락조건을 명확하게 나타내어야 합니다.
- 저작권자로부터 별도의 허가를 받으면 이러한 조건들은 적용되지 않습니다.

저작권법에 따른 이용자의 권리는 위의 내용에 의하여 영향을 받지 않습니다.

이것은 [이용허락규약\(Legal Code\)](#)을 이해하기 쉽게 요약한 것입니다.

[Disclaimer](#)

공학박사 학위논문

**Hyaluronic Acid Based Nanocomposite
Hydrogels Functionalized via
Nanoparticles for Biomedical
Applications**

나노입자를 통해 기능성을 부여한
생체의료용 히알루론산 기반 나노복합체
하이드로젤

2021년 8월

서울대학교 대학원

재료공학부

황 창 하

Hyaluronic Acid Based Nanocomposite Hydrogels Functionalized via Nanoparticles for Biomedical Applications

나노입자를 통해 기능성을 부여한 생체의료용
히알루론산 기반 나노복합체 하이드로젤

지도교수 김 현 이

이 논문을 공학박사 학위논문으로 제출함

2021년 8월

서울대학교 대학원

재료공학부

황 창 하

황 창 하의 박사 학위논문을 인준함

2021년 6월

위 원 장 안 철 희

부위원장 김 현 이

위 원 선 정 윤

위 원 한 철 민

위 원 정 현 도

Abstract

**Hyaluronic Acid Based Nanocomposite
Hydrogels Functionalized via
Nanoparticles for Biomedical
Applications**

Changha Hwang

Department of Materials Science and Engineering

Seoul National University

Hydrogel, a three dimensional network of hydrophilic cross-linked polymer, has received much attention for biomedical applications because of versatile advantages such as good biocompatibility and capability of tuning various properties. Among various polymers, hyaluronic acid (HA), which is a natural polysaccharide existed in human body, has extensively studied in recent years for a backbone of hydrogel due to excellent biocompatibility. However, weak mechanical properties and lack of various functions has been recognized

as major drawbacks of HA. Herein, the nanocomposite hydrogel system has been introduced as one of best candidates to overcome these limitations. Incorporation of nanomaterials in the hydrogel matrix not only enhance the mechanical property, but also endow functionality required in biomedical applications.

In the first study, we developed mechanically stable and highly lubricous hyaluronic acid-silica (HA-SiO₂) nanocomposite coatings through a sequential process consisting of a sol-gel method followed by electrophoretic deposition (EPD). SiO₂ nanoparticles, which the average diameter was about 90 nm, were uniformly dispersed in the HA-SiO₂ coating layer, and the nanocomposite coating thickness was confirmed as approximately 1-2 μm regardless of SiO₂ contents. Incorporation of SiO₂ nanoparticles into the HA polymer matrix enhanced the mechanical stability of the nanocomposite coatings, indicating higher adhesion strength compared to HA coating layers alone. Moreover, the nanocomposite coatings showed excellent biolubrication properties, which were evaluated with a customized tribological experiment on PDMS substrate. It is confirmed that the HA-SiO₂ nanocomposite has a great potential as a solution in biomedical devices that requires superior biolubrication performance.

In the second study, we fabricated reactive oxygen species (ROS) self-

generating hyaluronic acid hydrogel platform (HCZ hydrogel) via catechol-zinc oxide (ZnO) complexes for enhanced antibacterial therapy. Catechol-ZnO complexes enhanced ROS generation via the electron transfer during the formation of complexes, and created the hydrogel structure by coordination bonds between functionalized catechol groups in HA and ZnO nanoparticles simultaneously. This hydrogel demonstrated different behaviors in terms of mechanical characteristics compared with chemically cross-linked HA hydrogel containing ZnO nanoparticles (HAZ hydrogel). HCZ hydrogels showed higher swelling ratio, enzymatic degradation resistance, and tissue adhesive strength compared with the HAZ hydrogel. Hence, enhanced ROS generation from HCZ hydrogels was evaluated using electron paramagnetic resonance (EPR), H₂O₂ concentration, glutathione depletion, and intracellular ROS detection. Although ROS was generated from HCZ hydrogels, HCZ hydrogels showed no cytotoxicity except HCZ 10 (10 wt% of ZnO nanoparticles), which indicates low concentration of ZnO nanoparticles did not affect the cellular response. The improved antibacterial performance of HCZ hydrogels was also confirmed with *in vitro* and *in vivo* bacteria test against two bacteria strain (*E.coli* and *S.aureus*). Overall, the potential of the hydrogel created via catechol-ZnO complexes for the antibacterial therapy was demonstrated by the capability to produce lots of ROS and eradicate the bacteria.

In conclusion, these researches supported the incorporation of various nanoparticles in the HA hydrogel matrix potentially enhanced mechanical properties and assigned additional functionalities for biomedical applications. Improved mechanical stability and biolubrication performance of coating was obtained by the fabrication of HA-SiO₂ nanocomposite hydrogel coating. In addition, enhanced antibacterial performance of hydrogels was achieved via increased ROS generation from catechol-ZnO coordination complexes.

Keywords: Hydrogel; Hyaluronic acid; Nanocomposite hydrogel; Silica nanoparticle; Biolubrication; Zinc oxide nanoparticle; Catechol; Reactive oxygen species; Antibacterial property;

Student number: 2017-21069

Contents

Abstract	i
List of tables	x
List of figures	xi
Chapter 1. Introduction (Theoretical review).....	1
1.1. Hydrogel scaffolds for biomedical applications	2
1.2. Hyaluronic acid for hydrogel scaffold	3
1.3. Nanocomposite hydrogels	5
Chapter 2. Enhanced mechanical stability and lubrication performance for biomedical devices using hyaluronic acid-silica nanocomposite hydrogels	9
2.1. Introduction	10

2.2. Materials and Methods	13
2.2.1. Materials	13
2.2.2. Fabrication of the nanocomposite coatings	13
2.2.3. Characterization of the HA-SiO ₂ nanocomposite coating on SUS.....	14
2.2.4. Micro-scratch test.....	15
2.2.5. Friction test.....	16
2.2.6 Statistical analysis	16
2.3. Results & Discussion	17
2.3.1. Characterization of HA-SiO ₂ nanocomposite coatings.....	17
2.3.2. Adhesion strength of HA-SiO ₂ nanocomposite coatings.....	21
2.3.3 Friction test with PDMS substrate	22

2.4. Conclusions.....25

**Chapter 3. Antibacterial hydrogel with catechol-zinc
oxide nanoparticle coordination complex via enhanced
reactive oxygen species generation.....35**

3.1. Introduction36

3.2. Materials and Methods.....39

3.2.1. Materials39

3.2.2 Synthesis and characterization of catechol modified
hyaluronic acid (HA-CA)39

3.2.3. Preparation of ZnO nanoparticles40

3.2.4. Fabrication of HCZ hydrogel samples.....41

3.2.5. Characterization of hydrogels.....41

3.2.6. Swelling and degradation behavior	43
3.2.7. Rheological behavior.....	44
3.2.8. Tissue adhesion strength.....	44
3.2.9. Antibacterial activity of hydrogels	45
3.2.10. Intracellular reactive oxygen species (ROS) detection	46
3.2.11. Oxidative stress measurement via glutathione (GSH) depletion	47
3.2.12. H ₂ O ₂ generation measurement	47
3.2.13. <i>In vitro</i> cytotoxicity	48
3.2.14. <i>In vivo</i> antibacterial performance	49
3.2.15. Statistical analysis.....	51
3.3. Results and discussion.....	51

3.3.1. Synthesis and characterization of HCZ hydrogels	51
3.3.2. Measurement of enhanced ROS generation	57
3.3.3. <i>In vitro</i> cytocompatibility and antibacterial performance....	59
3.3.4. <i>In vivo</i> antibacterial performance of HCZ hydrogels	62
3.4. Conclusions	64
Chapter 4. Conclusions	80
4.1. Conclusions	81
References	84
초록 (Abstract)	106

List of tables

Table 2.1. Experimental conditions, zeta potential and silica contents of each sample

Table 2.2. The average surface roughness of HA, HA-Si10, HA-Si20, and HA-Si30 coatings

List of figures

Figure 1.1. Hyaluronic acid chemical structure and its biomedical applications (Redrawn from ref [34,35])

Figure 1.2. Schematic representation of the fabrication and advantages of nanocomposite hydrogels (Redrawn from ref [32, 36-39])

Figure 2.1. (A) Schematic illustration of the electrophoretic deposition method and structures of the HA-SiO₂ nanocomposite coating. (B) FT-IR spectra of the samples and XPS spectra of the (C) HA and (D) HA-Si₂₀ nanocomposite coating layer.

Figure 2.2. TGA graph to determine the SiO₂ content of HA-SiO₂ nanocomposite coatings

Figure 2.3. SEM images revealing the morphology of (A) HA, (B) HA-Si₁₀, (C) HA-Si₂₀, and (D) HA-Si₃₀ nanocomposite coatings in low and high magnification (inset) and (E) size distribution of SiO₂ nanoparticles of HA-Si₂₀

Figure 2.4. AFM images of (A) HA, (B) HA-Si₁₀, (C) HA-Si₂₀, (D) HA-Si₃₀

Figure 2.5. (A) Cross-sectional SEM image of HA-Si₂₀ and (B) coating thickness as a function of SiO₂ concentrations

Figure 2.6. Micro-scratch test on the HA and HA-SiO₂ nanocomposite coatings. SEM images of scratch tracks for the (A) HA, (B) HA-Si₁₀, (C) HA-Si₂₀, and (D) HA-Si₃₀ coatings on SUS. (E) Critical load of HA and HA-SiO₂

nanocomposite coatings (*: $p < 0.05$, **: $p < 0.005$, yellow arrow: complete delamination point)

Figure 2.7. (A) Schematic representation of the tribological experiment. (B) Coefficient of friction as a function of cycles and (C) average CoF value of HA and nanocomposite coatings (*: $p < 0.05$, **: $p < 0.005$)

Figure 3.1. Schematic illustration about the mechanism of enhanced ROS generation through catechol-ZnO complexes

Figure 3.2. Schematic diagrams of (A) synthesis of HA-CA polymer, $^1\text{H-NMR}$ spectra of (B) HA and (C) HA-CA polymer. (D) Absorbance spectra of dopamine solution with different concentrations and HA-CA

Figure 3.3. (A) TEM images of ZnO nanoparticles in low (Scale bar = 100 nm) and high resolution (Inset, scale bar = 10 nm). (b) Size distribution of ZnO nanoparticles

Figure 3.4. (A) Schematic illustrations of the preparation of HCZ hydrogel. (B) Phase transition of HCZ hydrogel, and (C) optic images of HAZ (left) and HCZ hydrogel (right)

Figure 3.5. SEM images of lyophilized (A) HAZ, (B) HCZ 3, (C) HCZ 5, and (D) HCZ 10 hydrogels (Scale bar = 40 μm)

Figure 3.6. (A) XRD patterns, (B) FT-IR spectra, and (C) UV-vis absorbance spectra of HAZ and HCZ hydrogels

Figure 3.7. High resolution XPS spectra of the carbon region (C 1s) for (A) the ZnO nanoparticles, (B) HA-CA, and (C) HCZ hydrogel respectively.

Figure 3.8. Characterization of HCZ hydrogels: (A) Rheological behavior represented from storage modulus for a frequency sweep mode. (B) Swelling ratio of the hydrogels for different time periods, 4, 7, 24, 48, 72 h. (C) In vitro enzymatic degradation behavior of the hydrogels in the presence of hyaluronidase. (D) Tissue adhesive strength of the hydrogels calculated from lab shear strength. (*: $p < 0.05$)

Figure 3.9. (A) EPR spectrum of ZnO, HAZ, and HCZ. (B) H₂O₂ concentration generated from HAZ and HCZ hydrogels with different ZnO amounts. (C) Optic images of color change of GSH after the hydrogel immersion at 37 °C for 0 h and 3 h respectively. (Scale bar: 2 cm) (D) Loss of GSH level after treating with hydrogels for 3 h.

Figure 3.10. (A) CLSM images of cultured HDF cells attached on HAZ and HCZ hydrogels. (B) Relatively cell viability evaluation of HAZ and HCZ hydrogels after 24 h culturing in HDF cells. (Scale bar: 200 μ m, *: $p < 0.05$)

Figure 3.11. (A) Disk diffusion test images against *E. coli* and *S. Aureus* of HAZ and HCZ hydrogels. (Scale bar: 20 mm) (B) Bactericidal efficacy of hydrogels against both bacteria strain after 24 h incubation. (*: $p < 0.05$) (C) The level of

intracellular ROS generation in *S.Aureus* after treatment with HAZ and HCZ hydrogels. (*: $p < 0.05$)

Figure 3.12. Morphology of *E.coli* and *S.aureus* attached on the surface of the hydrogels. (Scale bar: 1 μm)

Figure 3.13. (A) Schematic experimental designs of *in vivo* bacterial infection model in the subcutaneous skin of mouse. (B) Colony formation after treating with the hydrogels for 2 days, and (C) calculated count of colonies for each specimen. (*: $p < 0.05$)

Figure 3.14. (A) Representative histological sections images of *S. aureus*-infected skin lesions with H&E stain. (Original magnification: x40-Scale bar=500 μm , Original magnification: x400-Scale bar= 50 μm) (B) Mean abscess area (mm^2), (C) mean bacterial band length (mm), and (D) density of cellularity (%) from H&E stain sections. (*: $p < 0.05$)

Figure 3.15. Analysis of peripheral blood profiles in control, HAZ, HCZ3, and HCZ 10 mice at the time of sacrifice: (A) Proportion of neutrophils, lymphocytes, monocytes, eosinophils, and basophils in whole blood samples. (B) Absolute WBC counts, (C) Neutrophils counts, and (D) c-reactive protein (CRP) level. (*: $p < 0.05$)

Chapter 1.
Introduction
(Theoretical review)

1.1. Hydrogel scaffolds for biomedical applications

Over the past decades, tissue engineering which restores the functions of impaired tissues and organs in human body has extensively attracted widespread interest as the aging population increases [1]. Three factors including scaffolds, cells, and biological factors are the main components of tissue engineering [2]. Among these factors, scaffolds, which is defined as three-dimensional porous biomaterials, is essential for supporting extracellular matrix (ECM) deposition and cellular responses such as cell attachment, proliferation, and differentiation [3]. Numerous scaffolds are utilized to replace or recover the damaged tissues such as wound dressing, spinal fusion, stent, hip replacement, and artificial cartilage [4-6]. However, a few limitations have been recognized as a challenge to overcome for better tissue scaffolds. Relatively low biocompatibility and risk of bacterial infection could delay the tissue regeneration, and weak lubrication property could induce the tissue damage where the friction force between scaffolds and tissue occurs [7, 8].

Hydrogel scaffolds for tissue engineering have been considerably studied to solve these limitations because they have a similar structure with ECM of mammalian tissues [9]. Hydrogels are defined as three-dimensional networks of cross-linked hydrophilic polymer [10]. They absorb more than 90 % of water or biological media by weight which results in their great

biocompatibility [11]. In addition, the ability to tune the mechanical, chemical, and electrical properties easily is also the advantage of hydrogels for adopting to various biomedical applications such as wound dressing, drug delivery, 3D printing, and medical device coating [12]. The general polymers for hydrogels are classified into two major categories as synthetically and naturally existed polymers [13]. Although many synthetic polymers including poly(vinyl alcohol) and poly(ethylene glycol) are available to fabricate hydrogels, less biocompatibility compared with naturally existed polymers restricts the usage for biomedical scaffolds [14, 15]. Hence, naturally existed polymer, obtained from the natural ECM, has been recognized as the best candidate for the backbone of hydrogels due to its biocompatibility and biodegradable nature [16].

1.2. Hyaluronic acid for hydrogel scaffold

Hyaluronic acid (HA) is a well-known fascinating natural polysaccharide, which composed of two repeated units of D-glucuronic acid and N-acetyl-D-glucosamine. It abundantly existed in many soft tissues of human body like skin, synovial fluid, and vitreous humor, which results in the excellent biocompatibility, biodegradability, non-immunogenicity, and high lubrication property. Furthermore, HA actively plays a key role to regulate the

cell attach, migration, morphogenesis, and tissue regeneration [17]. Due to its outstanding characteristics, HA has been recently introduced to synthesize hydrogels for tissue engineering. It has been demonstrated that HA hydrogel enhances the biological functions in wound dressing, cartilage repair, and cell encapsulation (Figure 1.1) [18]. To fabricate the cross-linking system, chemical modification of HA is generally adapted because it has three targeted functional groups such as carboxylic acid, primary and secondary hydroxyl groups, and N-acetyl group [19]. Especially, carboxylic acid groups are dominantly modified to other functional groups which are available for the photo or chemically cross-linking [20]. With these advantages, the HA hydrogel has several drawbacks like weak mechanical properties and limited functions required for biomedical engineering [21].

To reinforce the mechanical properties, double network hydrogel systems are presented, which consists of two interpenetrating polymer networks in one hydrogel [22, 23]. A high degree of cross-linking chain determines the robustness of hydrogel, and the other cross-linking network endows the flexibility and toughness for the hydrogel. Double network hydrogels allow to dissipate energy from the rigid polymer chain, whereas the flexible polymer chain act to maintain the original state of hydrogels. In this way, this system enables to improve the mechanical strength compared with a single polymer

chain. Yang Qiao et.al designed a double network HA based hydrogel with folic acid and Fe^{3+} [24]. Coordination bonds of metal-carboxylate groups created the first network, followed by the formation of second network via UV radiation to the acrylamide-modified HA. This hydrogel enhanced mechanical strength and self-recovery properties due to increase of dissipated energy. Lihui Weng et.al also reported mechanically robust double network HA hydrogel combined with N,N-dimethylacrylamide cross-linking via UV radiation [25]. Although double network hydrogels are eminent in terms of mechanical strength, restricted physical and biological functions still remain a major challenge for the HA hydrogel.

1.3. Nanocomposite hydrogels

To overcome the challenges, a number of researches about “nanocomposite hydrogel” have been issued for the biomedical applications [26, 27]. The nanocomposite hydrogel is defined as the hydrogel combining with various nanomaterials such as graphene [28], carbon nanotube [29], metallic nanoparticles (iron oxide, silver, gold, titanium oxide, zinc oxide, copper oxide) [30], and ceramic nanoparticles (silica, bioactive glass, calcium phosphate, hydroxyapatite) [31]. The mechanical, chemical, electrical, and biological functions of nanocomposite hydrogels are facilitated to improve by

the original characteristics of nanomaterials and synergetic effects between polymer matrix and nanomaterials (Figure 1.2). Especially, in case of nanoparticles, the necessary multifunctions are easily inserted depending the type of nanoparticles for the desired biomedical applications. It is reported that the incorporation of carbon nanotube in collagen hydrogels enhanced the cellular activity as well as the mechanical strength [32]. Reinforced antibacterial property of alginate-HA hydrogels was also announced using the incorporation of silver nanoparticles [33].

Herein, we have focused on the HA hydrogel functionalization via two different types of nanoparticles for compensating the drawbacks of HA. In Chapter 2, HA-silica (HA-SiO₂) nanocomposite hydrogel coating system is proposed through in situ sol-gel process for a hydrophilic coating of biomedical devices. Enhanced mechanical stability and biolubrication performance of HA-SiO₂ compared with HA coating are systematically demonstrated. In Chapter 3, catechol-zinc oxide (ZnO) nanoparticle complexes based HA hydrogel is introduced for promoting the antibacterial performance. In this system, ZnO nanoparticles act as a cross-linker and antibacterial agents simultaneously. Moreover, the interaction between catechol groups and ZnO nanoparticles generated more reactive oxygen species which induces the bacteria eradication.

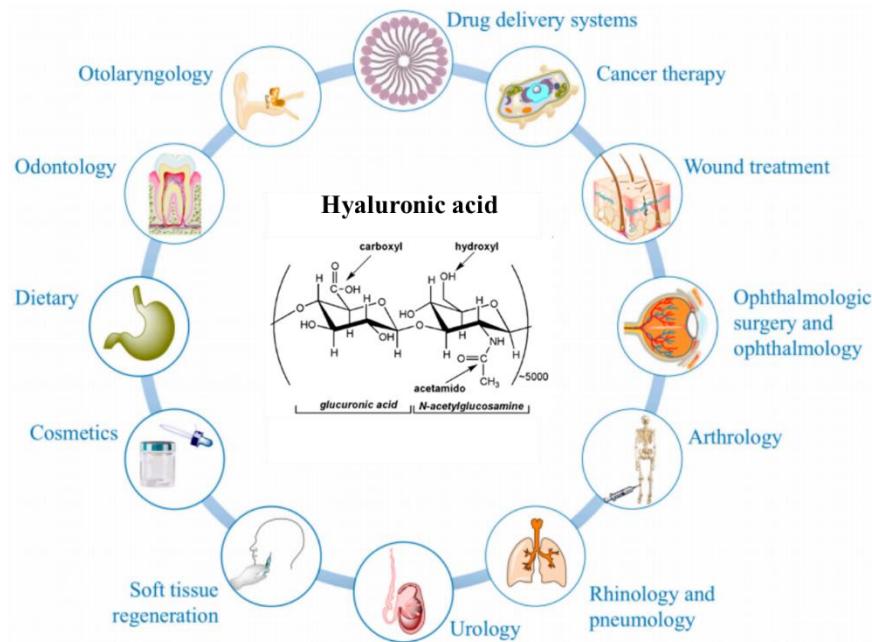


Figure 1.1. Hyaluronic acid chemical structure and its biomedical applications
 (Redrawn from ref [34, 35])

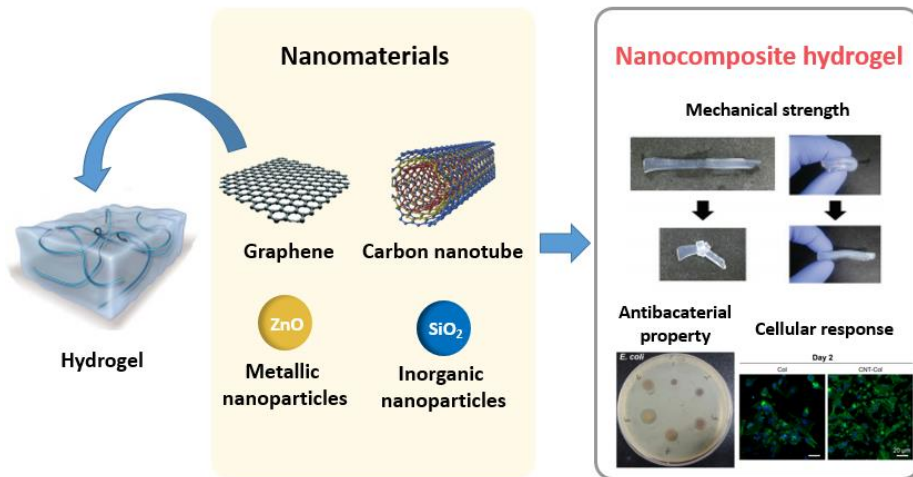


Figure 1.2. Schematic representation of the fabrication and advantages of nanocomposite hydrogels (Redrawn from ref [32, 36-39])

Chapter 2.

Enhanced mechanical stability and lubrication performance for biomedical devices using hyaluronic acid-silica nanocomposite hydrogels

2.1. Introduction

Hydrophilic coating is an important issue for a variety of biomedical applications such as articular cartilage, hip joint replacement, and intravascular guidewire [40, 41]. It can improve the biocompatibility of the biomedical devices and prevent immune responses under physiological environment. Previous works have suggested that hydrophilic polymers such as chitosan [42-44], heparin [45], alginate acid [46] and hyaluronic acid [42] are superior to decrease the friction force which induces the tissue damage occurring at interface regions between tissue and the coating layers of the implanted device, due to creation of hydration layers, resulting enhanced lubrication [47, 48]. Among those hydrophilic polymers, hyaluronic acid (HA) is a well-known polysaccharide which is abundant in bone marrow skin, and natural synovial fluid [49, 50]. It is an essential extracellular component that regulates the biological functions such as cell differentiation, and cell viability [51]. It also shows the lubrication performance in the human body owing to the high hydration ability [26]. Therefore, it has been extensively studied to apply to the lubrication coating of the biomedical devices [43, 52].

A variety of different techniques, including dip coating, spin coating, spray coating and electrophoretic deposition (EPD), are widely recognized to fabricate hydrophilic coatings on metal substrates [44, 53]. EPD has been well-

documented to generate the coating layers on the conducting substrate with not only colloidal particles, but also charged polymers like polysaccharides [54, 55]. The major advantages of this process are easily to create thin films on the complex three dimensional structures and control the coating thickness along with simply changing voltage and time of electric field. A. Simchi et al. discussed the EPD of chitosan which is a biocompatible cationic polysaccharide in terms of the pH dependent mechanism [56]. In addition, R. Ma et al. reported the EPD of HA and HA-bovine serum albumin with mechanism of deposition and microstructure of the films. However, there still remains requirements for enhancing the mechanical stability of HA as the coating material, thus certain physical or chemical anchoring systems are required. Physical adsorption of only polymers on metal substrates does not give a substantial stability due to a disparity between metal and polymer. This also decreases the lubrication performance because the polymer is readily detached from the substrate.

To improve the low coating stability, hybrid networked organic-inorganic materials are numerously investigated because it can combine the advantages of each component such as optical, mechanical, and thermal properties [57-59]. Herein, we introduce sol-gel mediated HA- silica (SiO_2) nanocomposite hydrogel coating using EPD for potential use as enhanced biolubricant coating materials on biomedical metallic implants. SiO_2 is one of

the best-known materials produced by the sol-gel process and frequently utilized for biomedical devices because it is highly biocompatible and bioactive, and it can establish strong structural stability in organic-inorganic network. During EPD, anionic HA chains and anionic silica sol are expected to form a structurally organized silica network in the HA hydrogel coating layer at the anode surface. In the previous research, HA polymer and discrete silica nanoparticles were electrodeposited, and the researchers only address the possible process of fabrication of organic-inorganic nanocomposites [60]. In this study, we are newly characterized lubrication properties and the coating stability of our homogenous HA-silica nanocomposite hydrogel materials. The surface characteristics such as morphology, chemical composition, average roughness (Ra) and coating thickness were investigated. Moreover, the interfacial strength and tribological behaviors were revealed with correlation of nanocomposite structures.

2.2. Materials and Methods

2.2.1. Materials

HA sodium salt with a molecular weight of 1.8-2.5 MDa was purchased from SK Bioland, Cheonan, Korea. Tetraethyl orthosilicate (TEOS), ammonium hydroxide (NH₄OH), phosphate buffered saline (PBS) and 1,4 butanediol diglycidyl (BDDE) were provided by Sigma-Aldrich.

2.2.2. Fabrication of the nanocomposite coatings

For the EPD technique, stainless steel 316L (SUS) alloy specimens were utilized as a substrate. Substrates were prepared with dimensions of 10 mm x 10 mm x 2 mm. The specimens were polished with abrasive SiC papers from 400 to 2000 grit, cleaned with ethanol in an ultrasonic bath, and dried in a 70 °C oven. A coating solution was prepared by mixing HA and TEOS. Afterwards, an HA-SiO₂ nanocomposite coating was fabricated by the sol-gel process. Briefly, solutions of HA in ethanol and TEOS with various amounts were prepared. To produce SiO₂ nanoparticles in the solution, distilled water, NH₄OH and BDDE for crosslinking HA were added to the solution. The solution was stirred vigorously at room temperature overnight. The final concentration of HA was 2 mg/ml. The experimental conditions are outlined in

Table 2.1. A platinum (Pt) electrode was used, and the distance between the substrate and the electrode was fixed at 15 mm. The EPD was conducted under a constant voltage at 20 V for 1 min. After the process, the coatings were obtained on SUS substrate and dried in a 37 °C oven for 24 h to remove the solvent.

2.2.3. Characterization of the HA-SiO₂ nanocomposite coating on SUS

The morphology of hydrogel coatings was observed using field emission scanning electron microscopy (FE-SEM, SUPRA SSV, Germany). Before observation, the hydrogel coatings on the substrate were dried at 37 °C for 1 day and then coated with Pt for electrical conduction. To verify the surface roughness, topographical examination was performed using atomic force microscopy (AFM, PAFM NX, EM4SYS Co. Ltd., Korea) under contact mode and ambient conditions. The size of the examined region was 10 μm x 10 μm. The cross-sectional image and thickness of coatings in a variety of conditions, such as SiO₂ content, polymer concentration, and deposition time, were investigated using a focused ion beam (FIB, Hellios 650, USA). To measure the amount of SiO₂ nanoparticles in the samples, thermogravimetric analysis (TGA, SDT Q600, USA) was performed using detached films from the substrate by

heating the samples to 600 °C at a rate of 10 °C/min in an O₂ atmosphere. The chemical structures of the coatings were identified by attenuated total reflectance Fourier transform infrared spectroscopy (FT-IR, Nicolet 6700, Thermo Scientific, USA) for wavenumbers ranging from 600 to 4000 cm⁻¹ with an average of 32 scans. X-ray photoelectron spectroscopy (XPS) was performed using a spectrometer (AXIS-His, Kratos, Japan) equipped with a monochromatic Al-K α X-ray source for characterizing the surface chemical composition. To check the stability of colloidal samples, zeta potential was investigated using a dynamic light scattering spectrometer (DLS, ELSZ 1000ZS size and zeta-potential analyser, Japan). Zeta potential was obtained from the pH 7 solution containing the nanocomposites.

2.2.4. Micro-scratch test

A micro-scratch test was performed using a micro-scratch tester (APEX-2T, Bruker, Germany) to measure the relative mechanical adhesion strength of the HA and nanocomposite coatings. The normal force, which increased linearly from 0 to 150 mN, was applied on the coatings using a Rockwell C diamond stylus indenter with a radius of 12.5 μ m. The total crack length and scratch speed were fixed at 500 μ m and 3 μ m/s, respectively. The tangential friction force was measured during the experiments, and the scratch

track was identified using FE-SEM. All scratch tests were conducted three times with each coating.

2.2.5. Friction test

The friction coefficient of the nanocomposite coatings was investigated using the custom-built reciprocating type tribometer [61]. The normal load was 50 mN, and the sliding speed was 2 mm/s for 150 cycles at room temperature in an aqueous condition. Polydimethylsiloxane (PDMS) at a 10:1 (w/w) ratio of the base and curing agent was utilized as a substrate. A 5 mm stainless steel ball with HA-SiO₂ nanocomposite coatings was utilized as the tip. Before each tribological test, the coatings were immersed in PBS solution for 10 min. The friction test was performed for each condition triplicate. In each experiment, new balls and PDMS substrates were used.

2.2.6 Statistical analysis

All experimental results were expressed as the mean \pm standard deviation (SD) with more than three specimens. The significant difference between the groups was evaluated using one-way analysis of variance (ANOVA), and comparisons with a p-value less than 0.05 were considered

statistically and significantly different (*p < 0.05).

2.3. Results & Discussion

2.3.1. Characterization of HA-SiO₂ nanocomposite coatings

Fabrication of the HA-SiO₂ coatings with the EPD technique is represented in **Figure 2.1A**. Briefly, in the process of solution preparation by sol-gel, TEOS, which is the precursor of SiO₂, was homogeneously dispersed in HA solution. After the base catalyst was added, SiO₂ nanoparticles were synthesized to create the hybrid network with HA. In addition, HA-SiO₂ was crosslinked by BDDE, which acts as a crosslinker under the basic condition [62], over time to form an organized nanocomposite structure. After the EPD process, the HA-SiO₂ nanocomposite hydrogel coating was obtained. This nanocomposite is fabricated as a hybrid structure with hydrogen bonding between the two components. The hydrogen bonding between HA and SiO₂ provides structural stability as a suspension state. Furthermore, these nanocomposite materials compared to a single polymer component can improve mechanical properties [63]. Therefore, HA-SiO₂ nanocomposite hydrogel coatings are effectively maintained even in aqueous solution. **Table 2.1** shows the amount of each precursor used to fabricate the nanocomposite coatings. All samples were produced in the ethanol-water solvent with a ratio

of 7:3 because this mixed solvent could promote the deposition of HA due to reduced electrostatic repulsion arising from the low dielectric constant of ethanol [64]. NH_4OH was added into the solution as a catalyst for the hydrolysis of TEOS, and BDDE was added as a crosslinker. The weight percentage of SiO_2 nanoparticles in every specimen was investigated using TGA analysis (**Figure 2.2**). The amount of SiO_2 in the HA-Si10, HA-Si20, and HA-Si30 was 9.67 ± 2.44 wt%, 21.73 ± 2.08 wt%, and 27.97 ± 1.38 wt%, respectively. This result indicated that the amount of SiO_2 nanoparticles in the solution increased proportionally with the concentration of TEOS.

Zeta potential was also monitored to indicate a driving force of EPD and colloidal dispersibility. This value represented the homogeneity and stability of nanocomposite suspensions, and it can provide a powerful imprint of interactions between polymer and nanoparticles such as electrostatic force and hydrogen bonding[65]. The zeta potential of HA is -52.4 ± 3.74 mV, suggesting favourable dispersibility and a negatively charged surface; hence, the zeta potential of nanocomposites is -60.75 ± 0.56 mV, -58.85 ± 0.97 mV, and -52.47 ± 1.22 mV. The HA- SiO_2 nanocomposite also had a negatively charged surface and was stable in the solution, which implies that this nanocomposite created one phase, including an organic and inorganic phase.

FTIR analysis was performed to characterize the chemical groups of

the nanocomposites, as shown in **Figure 2.1B**. HA peak was detected in all specimens corresponding to the stretching vibrations of hydroxyl group (O-H) located at 3000-3500 cm^{-1} . Moreover, alkyl group (C-H), carbonyl group (C=O), sodium carboxylate group (COO-), and primary alcohol group (C-O) were located at 2877, 1605, 1402, 1035 cm^{-1} respectively. Si peaks were identified for HA-SiO₂ nanocomposite coatings at 1074 cm^{-1} and 450 cm^{-1} which represents stretching vibration of Si-O-Si. Although the intensity of the carbonyl peak was slightly decreased, the intensity of the silica-related peak was much greater with increasing SiO₂ nanoparticle content. The surface chemical composition of the nanocomposites was investigated using XPS, as shown in **Figure 2.1C-D**. Wide scans of XPS spectra revealed C 1s, O 1s, N 1s, and Si 2p at 284.5, 530.9, 398, and 101.5 eV, respectively. High magnification of the Si 2p signal was obtained in HA and HA-Si20. While no Si 2p signal was detected from the HA coating, the Si 2p peak was identified in the HA-Si20 coating at 101.5 eV. This peak was expected to shift 2-3 eV higher in binding energy than the SiO₂ peak. This phenomenon occurs because of the interaction via hydrogen bonding between HA and SiO₂ nanoparticles, which creates different suboxide components (Si_xO₂) at the surface [66].

The surface morphology of all specimens can be observed in **Figure 2.3** using SEM. The HA coating shows no cracks and a smooth surface,

implying that the SUS substrate was covered entirely with the HA (**Figure 2.3A**). HA-SiO₂ nanocomposite coatings were created with uniformly dispersed SiO₂ nanoparticles, as shown in **Figure 2.3B-D**. The precursor of SiO₂ was homogeneously distributed in the HA-SiO₂ solution, and the nanoparticles started to grow from a spot of the precursors. Furthermore, when the contents of nanoparticles increased, the surface coverage area of SiO₂ also increased noticeably. The size of the nanoparticles was calculated in the range from 30 to 120 nm, and the average particle size was close to 90 nm, as indicated in **Figure 2.3E**.

The surface topography and average roughness values of HA-SiO₂ nanocomposite coatings are represented in **Figure 2.4**. The HA coating, as detailed in **Figure 2.4A**, could have a porous structure, which indicates that these coating systems were hydrogel. Although the HA-SiO₂ nanocomposite coatings also had a porous structure, it was difficult to find the pores due to the surface coverage by the SiO₂ nanoparticles. In **Figure 2.4B-D**, HA-SiO₂ nanocomposite coatings showed a similar structure in which the SiO₂ nanoparticles were distributed regardless of the amount, but the average roughness increased with the content of SiO₂. The average roughness value of each specimen is shown in **Table 2.2**. The roughness factor slightly increased

as the amount of SiO₂ nanoparticles increased, but regardless of the amount of SiO₂, all nanocomposite coatings had nanoroughened structures.

A cross-sectional image of the HA-SiO₂ nanocomposite coating was obtained as listed in **Figure 2.5A**. SiO₂ nanoparticles were incorporated uniformly from bottom to top. The measured coating thickness of all samples is shown in **Figure 2.5B**. The coating thicknesses of the HA and HA-SiO₂ coatings were 1.32±0.34 μm, 1.46±0.25 μm, 1.14±0.17 μm, and 1.16±0.04 μm. All coatings have similar coating thicknesses regardless of the amount of SiO₂. This suggests that the weight percentage of SiO₂ is not an important factor for drastically changing the thickness of the coating in the case of the EPD method.

2.3.2. Adhesion strength of HA-SiO₂ nanocomposite coatings

A scratch test was performed to characterize the mechanical properties in terms of adhesion strength between the substrate and coatings. The mechanical adhesion strength can be identified with a critical load at which complete delamination occurred. As shown in **Figure 2.6A**, the delamination point occurred in the middle of the track for all coatings. However, the delamination point of the HA-SiO₂ nanocomposite coating was exposed later than the delamination point of the HA coating, which reveals that the

nanocomposite coatings have even higher adhesion strength. In addition, when the amount of SiO₂ increased, the distance from the starting point to the delamination part also increased proportionally. A critical load, which is the measured force when complete delamination of the coating occurred, was calculated from SEM images (**Figure 2.6B**). The critical loads of HA and HA-SiO₂ nanocomposite coatings were 41.07±0.34, 47.66±2.43, 54.31±0.41, and 58.48±0.50 mN. The highest value appeared for HA-Si30, which shows an approximately 42% greater critical load than the HA coating. These results imply that SiO₂ nanoparticles in the HA matrix enhance the adhesion strength of the coating because of electrostatic force and hydrogen bonding derived from the surface of SiO₂. This process is widely recognized to improve the adhesion strength of polymers. For instance, uniformly dispersed SiO₂ nanoparticles are utilized to improve the adhesion strength in the polyacrylate-silica nanocomposite structure [67]. This increased adhesion strength could improve the mechanical interlocking strength with the substrate and provide an anchoring effect to the HA [68, 69].

2.3.3 Friction test with PDMS substrate

A schematic illustration of the experimental tribological test model in this study is presented in **Figure 2.7A**. Due to its compliance, PDMS was

utilized as the substrate to reduce the contact pressure. Compliance of the substrate is an important factor in investigating the tribological behavior of soft coatings such as biofilms. Moreover, some researchers have already treated PDMS substrate for the soft-tribology system [70]. The reduced contact pressure of this experiment was calculated based on the Hertz contact model [71]. The elastic modulus and Poisson's ratio of SUS 316L were 193 GPa and 0.27, respectively [72]. The corresponding values of PDMS were estimated to be 2.61 MPa and 0.5, respectively [73]. Based on these figures, the calculated contact pressure was 0.18 MPa, which was given from the reduced elastic modulus (E^*) and a theoretical Hertz contact area radius.

All nanocomposite coatings were deposited on the SUS ball attached to the dispenser. Afterwards, the coatings were immersed in the PBS buffer solution, which was placed on the PDMS substrate for 10 min before initiating the reciprocating experiment in order to maintain an equilibrium swelling state. **Figure 2.7B** shows the tendency of CoF as a function of cycles. The average CoF values of all coatings were 0.045 ± 0.005 , 0.032 ± 0.001 , 0.025 ± 0.001 , and 0.027 ± 0.004 , as displayed in Fig. 6C. As SiO_2 was incorporated, the CoF profile of the nanocomposite coatings was far smoother than the HA coating, and the CoF value significantly decreased in the stabilized sections of the graph. The tendency of the CoF value of all coatings could be related to the adhesion

strength of the nanocomposite coating. It has been reported that polymer coatings on hard nanoparticle surfaces have a low CoF value compared with smooth polymeric coatings [74]. According to **Figure 2.6**, the adhesion strength of the coatings increased with the incorporation of SiO₂. This strength increase could imply that the HA in the nanocomposite structure was robustly immobilized on the substrate by SiO₂ nanoparticles. Hence, it is suggested that the CoF value under physiological conditions is reduced by tethered polyelectrolyte polymers on the substrate due to a high grafting density [75]. HA is physically bound to SiO₂ nanoparticles via an electrostatic force and hydrogen bonding, and a higher polymer density on the substrate is obtained. It is assumed that HA is stretched away from the substrate by an electrostatic force formed between negatively charged polymers in a high grafting density structure [76]. This force could create a much thicker hydration layer, leading to more effective lubrication in the aqueous environment [75]. However, the CoF value of HA-Si30 was very similar to HA-Si20, even though the weight of SiO₂ increased. This result might suggest that the density of HA on the substrate was maximized at 20 wt% of SiO₂; thus, HA-Si20 and HA-Si30 show similar lubrication performance. Although the friction test was conducted for 150 cycles, no wear tracks were detected on all nanocomposite coatings. This result could suggest that the high lubrication property does not impact the creation of wear tracks.

2.4. Conclusions

HA-SiO₂ nanocomposite coatings were successfully fabricated on SUS substrates via the sol-gel method and EPD technique. The SiO₂ nanoparticles were uniformly distributed in the HA matrix, and the coatings had a nanoroughened structure regardless of the SiO₂ content. HA-SiO₂ coatings had relatively high interfacial strength compared to HA coatings because SiO₂ nanoparticles act as the binding agent with metal substrates. Furthermore, HA-SiO₂ nanocomposite coatings gradually reduced the CoF value along with the amount of SiO₂ in the aqueous environment because immobilized SiO₂ increases the grafting density of HA on the substrate. These results demonstrate that highly superior biolubricant coating systems can be achieved through the simple incorporation of SiO₂ nanoparticles into HA. These characteristics suggest that HA-SiO₂ nanocomposite coatings have great potential for use in the biolubricated coating of medical devices.

	EtOH: DW (V/V)	HA (mg/ml)	NH4OH (ml)	BDDE (μ l)	TEOS (ml)	Zeta potential (mV)	Silica contents (%)
HA	7:3	2	2.57	100	0	-52.39 \pm 3.74	0
HA-Si10					0.1	-60.75 \pm 0.56	9.67 \pm 2.44
HA-Si20					0.2	-58.85 \pm 0.97	21.73 \pm 2.08
HA-Si30					0.3	-52.47 \pm 1.22	27.97 \pm 1.38

Table 2.1. Experimental conditions, zeta potential and silica contents of each sample

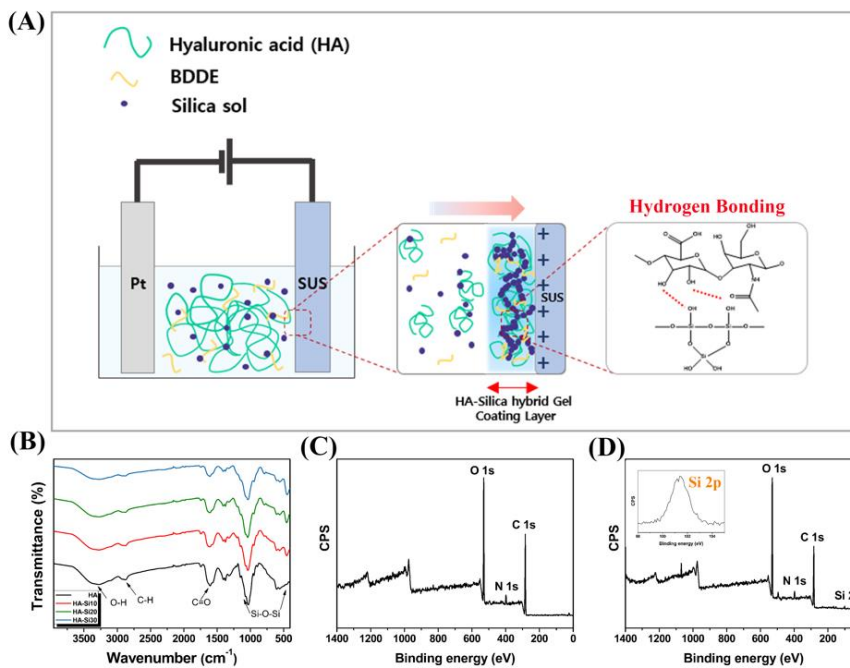


Figure 2.1. (A) Schematic illustration of the electrophoretic deposition method and structures of the HA-SiO₂ nanocomposite coating. (B) FT-IR spectra of the samples and XPS spectra of the (C) HA and (D) HA-Si₂₀ nanocomposite coating layer.

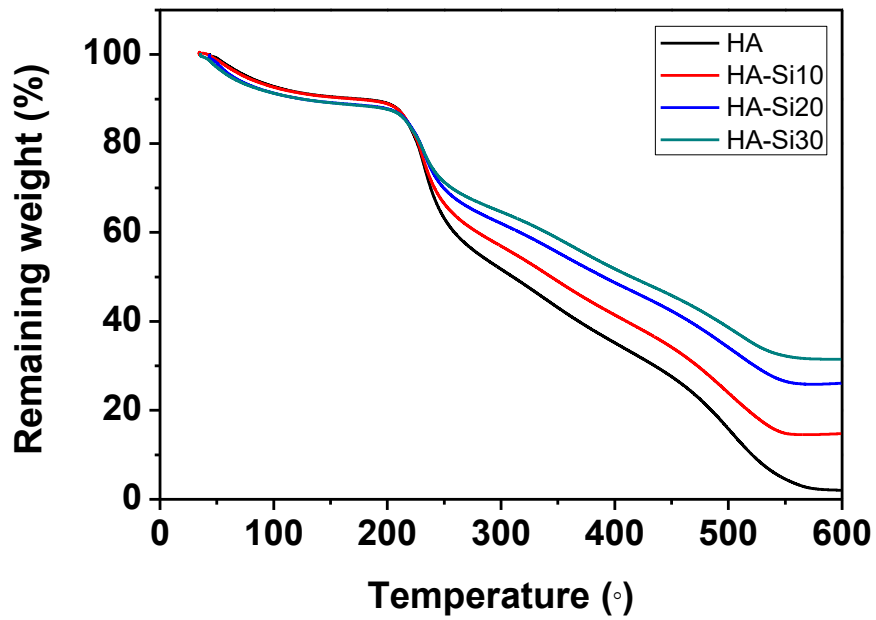


Figure 2.2. TGA graph to determine the SiO₂ content of HA-SiO₂ nanocomposite coatings

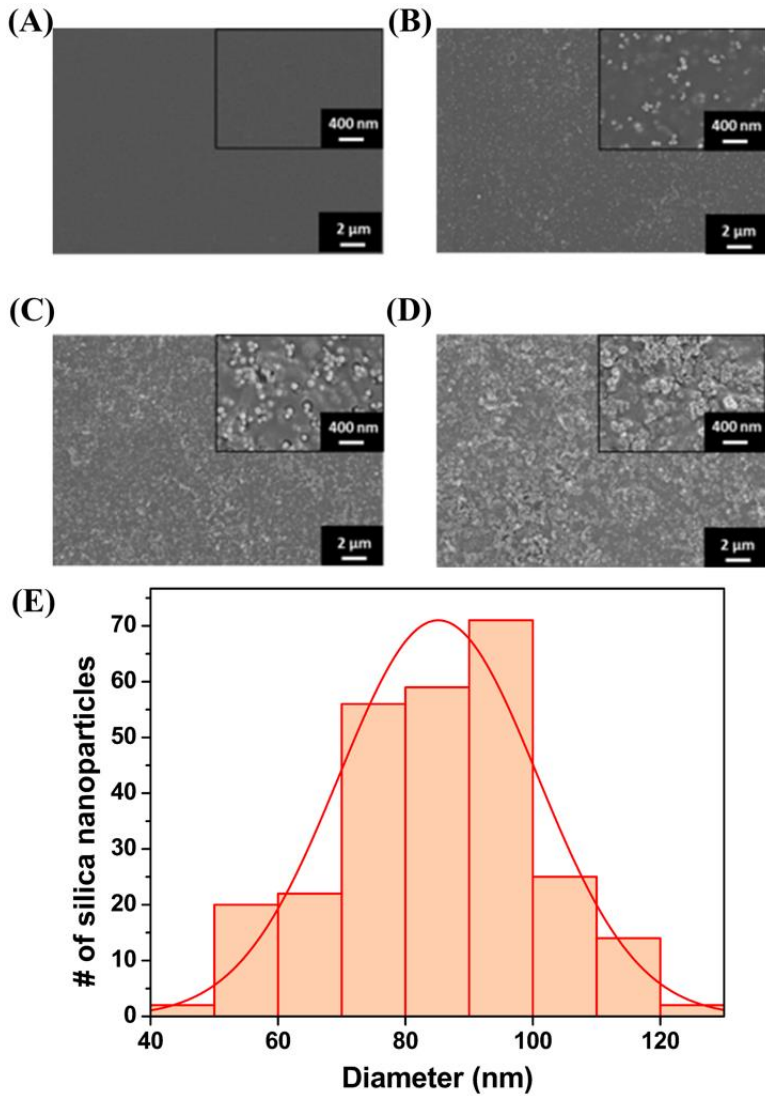


Figure 2.3. SEM images revealing the morphology of (A) HA, (B) HA-Si10, (C) HA-Si20, and (D) HA-Si30 nanocomposite coatings in low and high magnification (inset) and (E) size distribution of SiO₂ nanoparticles of HA-Si20

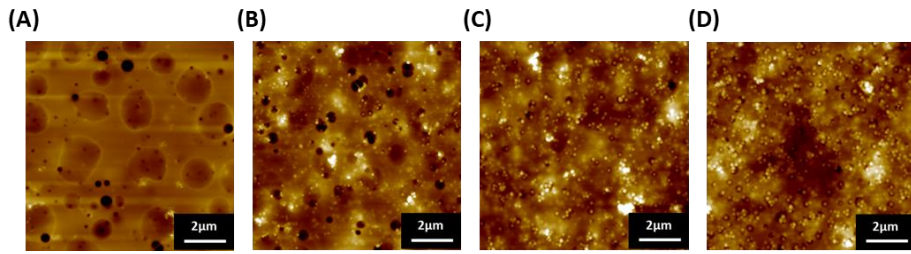


Figure 2.4. AFM images of (A) HA, (B) HA-Si10, (C) HA-Si20, (D) HA-Si30, and (E) the average surface roughness (R_a) of each sample

	HA	HA-Si10	HA-Si20	HA-Si30
$R_a(\text{nm})$	10 ± 4.1	24.6 ± 3.6	34.2 ± 5	39.9 ± 1.4

Table 2.2. The average surface roughness of HA, HA-Si10, HA-Si20, and HA-Si30 coatings

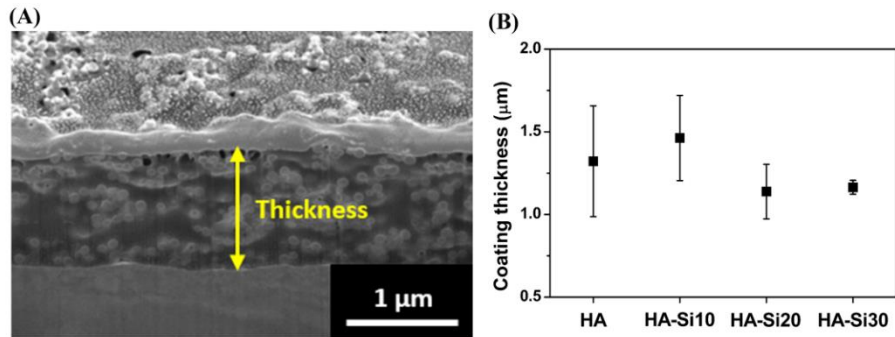


Figure 2.5. (A) Cross-sectional SEM image of HA-Si20 and (B) coating thickness as a function of SiO₂ concentrations

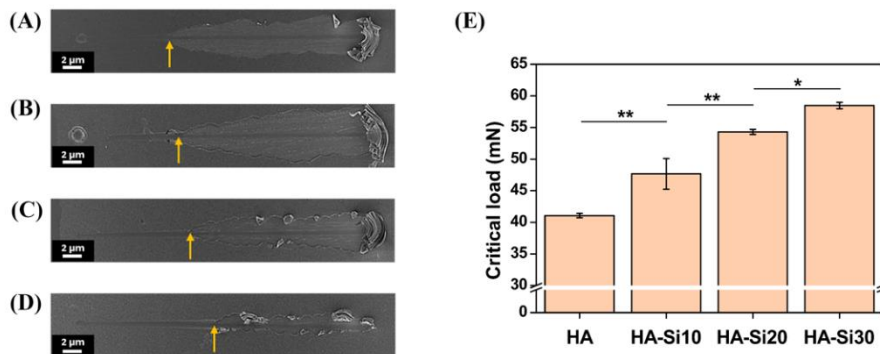


Figure 2.6. Micro-scratch test on the HA and HA-SiO₂ nanocomposite coatings. SEM images of scratch tracks for the (A) HA, (B) HA-Si10, (C) HA-Si20, and (D) HA-Si30 coatings on SUS. (E) Critical load of HA and HA-SiO₂ nanocomposite coatings (*: $p < 0.05$, **: $p < 0.005$, yellow arrow: complete delamination point)

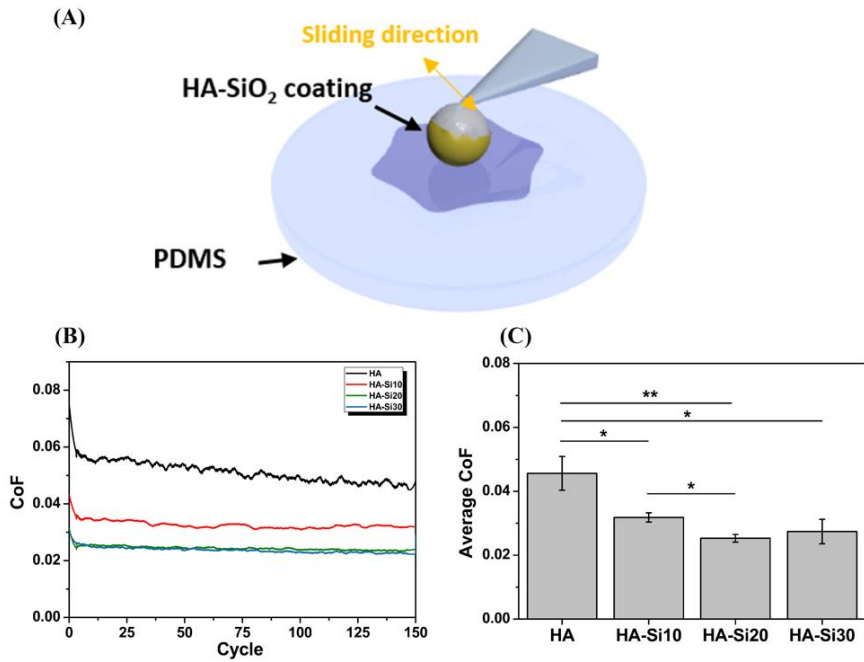


Figure 2.7. (A) Schematic representation of the tribological experiment. (B) Coefficient of friction as a function of cycles and (C) average CoF value of HA and nanocomposite coatings (*: $p < 0.05$, **: $p < 0.005$)

Chapter 3.

**Antibacterial hydrogel with catechol-zinc
oxide nanoparticle coordination complex via
enhanced reactive oxygen species generation**

3.1. Introduction

Reactive oxygen species (ROS) including hydroxyl radical ($\bullet\text{OH}$), singlet oxygen ($^1\text{O}_2$), superoxide anion ($\text{O}_2^{\bullet-}$), and hydrogen peroxide (H_2O_2) play essential roles in the biological functions such as cell cycle, homeostasis, and defense response [77, 78]. At low concentrations, ROS stimulates vascular reconstruction, cell migration, and wound healing process [78]. However, the excessive of ROS could induce the oxidative damages to cellular molecules [79]. Over the past decades, strategies based on the high levels of ROS generation have been introduced in a field of antibacterial therapeutics [79, 80]. The general approach in ROS generation for killing the bacteria is to utilize photocatalysts including metal oxide nanoparticles such as titanium oxide (TiO_2), copper oxide (CuO), and zinc oxide (ZnO) [81]. In particular, ZnO nanoparticles have shown a great promise as biomedical applications because of its distinct characteristics [82]. ZnO nanoparticles have a superior photocatalytic activity under light irradiation derived from its semiconductor structure and surface defects [83-85]. Moreover, Zn ions (Zn^{2+}) released from ZnO nanoparticles play an important role to regulate the cellular functions and kill the bacteria [86, 87]. However, ROS generation from ZnO nanoparticles is restricted to the external light intensity and penetration depth of light to the skin tissue, thus limiting the amount of ROS release as the antibacterial agents [88].

Catechol, a bioinspired source from the protein of marine mussels [89], is proposed as one of the best candidates for biomedical applications due to its biocompatibility and adhesive capacities on the surface of any materials [90, 91]. Recently, metal oxide nanoparticles have been introduced to form the metal-mediated catechol complexes due to obtaining synergetic properties from both metal oxide and catechol characteristics [92]. Anchoring ability of catechol with metal atoms on the surface of metal oxide nanoparticles establishes the reversible coordination bonds [93]. Furthermore, previous studies mentioned that metal-mediated catechol complexes produce ROS through the oxidation process [94]. The electron transfer during the oxidation from catechol to *o*-semiquinone which metal oxide nanoparticles act as a catalyst transforms oxygen molecules into ROS [95, 96]. ROS generation and metal ion release from metal oxide nanoparticles could affect the cellular response and antibacterial activity [97]. Therefore, we hypothesize that the catechol-metal oxide nanoparticle complexes could improve the efficacy of killing bacteria with increase of ROS generation rather than metal oxide nanoparticle itself.

To utilize the catechol-metal oxide nanoparticle complexes as ROS carriers in the form of implantable therapeutic nanoplatform, we introduce a hydrogel structure because high water content and porosity enable a delivery of

ROS to the physiological environment. This paper focuses on presenting the design of ROS releasing hydrogel cross-linked via catechol-ZnO nanoparticle complexes. Hyaluronic acid (HA), a natural polysaccharide existed in a human body, is utilized as a backbone of hydrogel because of its nonimmunogenic, biocompatible, and degradable nature [26]. The mechanism about enhancing ROS generation of catechol-ZnO complex based hydrogels is described in **Figure 3.1**. First, the catechol oxidation and semiquinone could transfer the electrons to oxygen molecules which occurs the formation of ROS. Furthermore, trapped electrons in the oxygen vacancy of ZnO nanoparticles attribute to transform the oxygen molecules into ROS. These two expected factors reveal the synergetic effects in terms of ROS production. In this system, ZnO nanoparticles act not only as the antibacterial therapeutic agents, but also cross-linker agents simultaneously. Coordination bonds between catechol and Zn atoms on ZnO nanoparticles can create cross-linking points of this hydrogel model. Hydrogel characteristics derived from coordination bonds between catechol and ZnO nanoparticles were examined. Additionally, the ability of ROS generation was determined using electron paramagnetic resonance (EPR), H₂O₂ concentration, glutathione (GSH) depletion, and intracellular ROS detection (DCFDA) assay. Enhanced antibacterial performance of the hydrogel was also demonstrated with both *Escherichia coli* (*E. coli*) and *Staphylococcus aureus* (*S. aureus*) strain using in vitro and in vivo experiments.

3.2. Materials and Methods

3.2.1. Materials

HA sodium salt with a molecular weight of 50-110 KDa was purchased from Pharmaline Co., (Suwon, Korea). Zinc acetate dihydrate (99.999% trace metals basis), sodium periodate, methanol, dopamine hydrochloride, 1-ethyl-3-(3-dimethylaminopropyl) carbodiimide hydrochloride (EDC), N-Hydroxysuccinimide (NHS), 1,4-butanediol diglycidyl ether (BDDE), dialysis tubing cellulose membrane (molecular weight cut off = 14,000), 5,5-dithio-bis-(2-nitrobenzoic acid) (DTNB), L-glutathione reduced (GSH), and hyaluronidase (Type I-S, lyophilized powder, 400-1000 units/mg solid) were purchased from Sigma Aldrich (St. Louis, USA).

3.2.2 Synthesis and characterization of catechol modified hyaluronic acid (HA-CA)

HA-CA was synthesized using an EDC/NHS coupling agents where the carboxyl groups of HA chain were reacted with the amine groups of dopamine. Briefly, 2 g of HA was dissolved in 100 ml of Dulbecco's Phosphate-

Buffered Saline (PBS) and the pH value of solution was adjusted to 5.5 using 1 M hydrochloric acid (HCl). EDC and NHS were added to the HA solution, followed by the addition of dopamine hydrochloride (DA). The final molar ratio of HA/EDC/NHS/DA was set to 1:1:1:1 and the mixed solution was stirred overnight at room temperature. After the reaction, the dialysis was conducted to remove unreacted dopamine for 2 days in pH 5.5 PBS solution and 4 hours in a distilled water, followed by the lyophilization. Synthesized HA-CA was stored at 4 °C until using at the experiment. The HA-CA was confirmed using ¹H-nuclear magnetic resonance (NMR) (Avance III-500, Bruker, German), and conjugated catechol ratio of HA-CA was determined by measuring absorbance at 280 nm using UV-vis spectroscopy (V-770, JASCO, USA) with a dopamine standard curve.

3.2.3. Preparation of ZnO nanoparticles

ZnO nanoparticles were synthesized by a precipitation method from the zinc acetate precursor. Briefly, 0.1 M zinc acetate dihydrate solution was prepared using methanol as a solvent. 1 M sodium hydroxide solution was added dropwise to the zinc acetate solution under vigorous stirring for 1 hour. The precipitated ZnO nanoparticles were obtained by centrifuge and washed several times using ethanol and distilled water. Finally, after drying the ZnO

powders at 70 °C, calcination was conducted at 500 °C for 1 hour.

3.2.4. Fabrication of HCZ hydrogel samples

For each hydrogel specimen, the ZnO nanoparticles were dispersed in distilled water and sonicated for 1 hour. After the sonication, 5 wt% of HA-CA was added to the ZnO solution and stirred until the polymer was fully dissolved. The final concentration of ZnO nanoparticles in the mixed solution was determined to 3,5, and 10 wt% compared with the amount of HA-CA. The mixed solution was transferred into a plastic mold and HCZ hydrogels were prepared after placing in 50°C for 24 h. The control hydrogel (HAZ hydrogel) was fabricated by chemical cross-linking system using BDDE including HA and ZnO nanoparticles. 5 wt% of HA in the 0.2 M NaOH with 3 wt% of ZnO nanoparticles was stirred, and mixed with 80 µl/ml of BDDE. The HAZ hydrogel was produced under 37 °C for 24 h.

3.2.5. Characterization of hydrogels

The morphology of HAZ and HCZ hydrogels was observed using field emission scanning electron microscopy (FE-SEM, SUPRA SSVP, Carl Zeiss Inc., Germany). Before observation, the hydrogels were prepared by the

lyophilization, followed by coating with platinum for electrical conduction. ZnO nanoparticles were analyzed using transmission electron microscopy (TEM, JEM-2100F, JEOL Ltd., Japan) with an accelerating voltage of 200 kV to identify the structure. The phase of the ZnO nanoparticles in the hydrogel was determined by X-ray diffractometer (XRD; D8-Advance, Bruker Co., Germany) with a scanning range of 20°-80° at a rate of 1°/min. X-ray photoelectron spectroscopy (XPS, AXIS SUPRA, Kratos, U.K) was conducted to confirm the chemical states of composing elements of HCZ using a monochromatic Al K α radiation. UV-visible light absorption spectra were characterized using UV-visible spectroscopy (V-770, JASCO, Japan) ranged from 260 nm to 800 nm. Zeta potential and particle size distribution were measured with a dynamic light scattering spectrometer (DLS, ELSZ 1000ZS size and zeta potential analyzer, Japan). The zeta potential and hydrodynamic diameter were obtained from diluted HA-CA solution containing ZnO nanoparticles. Electron paramagnetic resonance (EPR) measurement was conducted on an EPR spectrometer (EMXmicro-9.5/2.7, Bruker Co., Germany) at the X-band frequency (9.43 GHz). To verify the radical formation in this system, the mixed solution containing 20 mg/ml of ZnO nanoparticles and 10 mg/ml of HA and HA-CA polymer was utilized. Afterwards, a baseline correction processing of acquired spectra was performed using Win-eprocess software.

3.2.6. Swelling and degradation behavior

The equilibrium swelling ratio of HAZ and HCZ hydrogels was evaluated in PBS solution at 37 °C for each time point. Before swelling, the hydrogels were dried by lyophilization to obtain the initial weight (W_i). At certain time points, the weight of hydrogels was measured after removing excess of buffer solution. The swelling ratio of the hydrogels were calculated as

$$\text{Swelling ratio (g/g)} = (W - W_i) / W_i$$

where W_i and W are the weight of dried hydrogels and swollen hydrogels, respectively.

In vitro enzymatic degradation behavior was observed in PBS solution containing hyaluronidase which the concentration is 12.5 µg/mL (5-12.5 UI/mL) at 37 °C. The initial weight (W_i) was measured after 1 day swelling in PBS solution, and the remaining weight (W_r) was measured at each time interval in PBS with hyaluronidase solution. The remaining weight ratio was calculated using the following equation:

$$\text{Remaining weight ratio (\%)} = (W_r / W_i) * 100$$

3.2.7. Rheological behavior

The rheological behavior of the hydrogels was examined using a frequency sweep mode of a rheometer (TA,). All specimens were fabricated with a 20 mm diameter and a 2 mm thickness. The storage modulus (G') and loss modulus (G'') were confirmed under a constant strain (0.01) over the frequency range from 0.1 to 50 rad/s with 20 mm diameter parallel plates.

3.2.8. Tissue adhesion strength

Tissue adhesion strength measurement of HAZ and HCZ hydrogels was conducted to measure the adhesive strength between hydrogels and a porcine skin using universal testing machine (Instron 5543, Instron, USA) with a 50 N load cell. The porcine skins were purchased from a local slaughterhouse. Porcine skins were cut into 10 mm x 30 mm and immersed in PBS solution at 37 °C for 3 h to maintain the hydrate state. Hydrated porcine skins were attached onto the clear cover glass using a cyanoacrylate glue (loctite, Germany). The fabricated hydrogel samples were prepared with an area of 10 mm x 10 mm and deposited between two porcine skin substrates. Subsequently, the tissue adhesion strength was tested by a lab shear test method under the

constant cross-head speed of 3 mm/min. The maximum tensile strength divided by a joint area indicated the adhesion strength of hydrogels.

3.2.9. Antibacterial activity of hydrogels

To evaluate the antibacterial activity of the hydrogels, the hydrogels were subjected to two bacteria strains, *Escherichia coli* (*E. coli*, ATCC 8739, gram-negative) and *Staphylococcus aureus* (*S. aureus*, ATCC 6538, gram-positive), through an agar diffusion test and optical density (OD) value at 595 nm. 50 µl of *E. coli* and *S. aureus* were inoculated in 3 ml of fresh Luria-Bertani (LB) broth (BD Difco™, 244620, USA), followed by culturing overnight at 37 °C in a shaker under 200 rpm. To measure the OD value at 595 nm, 200 µl and 50 µl of prepared hydrogels were placed into the diluted *E. coli* and *S. aureus* solution which a concentration was 5×10^4 CFU/ml in the 12 well culture plate and cultured at 37 °C for 24 h, respectively. After that, 200 µl of treated bacteria suspension was collected in 96 well culture plate, and the OD at 595 nm was measured. For the agar diffusion test, 200 µl of diluted bacteria suspension was dropped and spread on the agar plate using triangular bar. 200 µl of prepared hydrogels were placed on the center of agar plate and then incubated at 37 °C for 24 h. The inhibition zone images were acquired using a digital camera. Morphological changes of bacteria were observed using FE-SEM on the surface

of hydrogel. The hydrogels were covered with 1×10^7 CFU/ml of both bacteria strain solutions at 37 °C for 3 h. The bacteria attached on hydrogels were fixed by 2.5 % glutaraldehyde for 10 min, and then dehydrated in 75 %, 95 %, and 100 % ethanol during 5 min for each process. Afterwards, the samples were immersed in hexamethyldisilazane for 10 min in 2 times, followed by an air dried.

3.2.10. Intracellular reactive oxygen species (ROS) detection

Levels of intracellular ROS generation were detected using 2',7'-dichlorofluorescein diacetate (DCFDA, Assaygenie, UK), which transforms into a fluorescent dye after diffusion into the cells. 50 µl of *S. aureus* were inoculated in 3 ml of fresh Luria-Bertani (LB) broth (BD Difco™, 244620, USA) at 37 °C in a shaker for overnight. Suspended *S. aureus* was collected by centrifuge at 4000 rpm and washed with PBS twice, followed by exposed to 25 µM of DCFDA for 45 min. Next, hydrogels were immersed into diluted *S. aureus* solution at the concentration of 1×10^7 CFU/ml for 3h in a dark. In the end, the fluorescence intensity was recorded by excitation of 485 nm laser and emission of 535/20 nm filter using a microplate reader (Victor 3, Perkin Elmer, USA). The fluorescence intensity is proportional to the amount of intracellular ROS.

3.2.11. Oxidative stress measurement via glutathione (GSH) depletion

To monitor the level of oxidative stress by ROS generation from hydrogels, GSH depletion was measured by quantifying the concentration of thiol groups after interacting with hydrogels by using Ellman's assay [98]. Typically, 200 μ l of hydrogels were immersed in 3 ml of GSH bicarbonate buffer solution (GSH, 1 mM; bicarbonate buffer, 50 mM, PH =8.7). After 3 h incubation at 37 $^{\circ}$ C, 50 μ l of bicarbonate buffer solution with DTNB (10 mM) was added into the GSH solution. The reacted solution was collected to measure the absorbance at 412 nm. Loss of GSH ratio was calculated with this equation: Loss of GSH [%] = (absorbance of negative control – absorbance of sample) / absorbance of negative control x 100. The negative control was GSH solution without any samples.

3.2.12. H₂O₂ generation measurement

To identify the concentration of H₂O₂ generated from HCZ hydrogels, the amount of H₂O₂ was quantified using a Quantative Peroxide Assay Kit (Pierce, Rockford, USA). Briefly, 200 μ l of the hydrogels was immersed in 3ml

of PBS solution for predetermined time intervals (3h, 6h, and 24h). Next, 20 μ l of each treated media was mixed with 200 μ l of assay kit reagent and incubated at room temperature during 20 min. The absorbance was measured at 595 nm on a microplate reader (EZ read 400, Biochrom, UK). The standard curve of H₂O₂ concentration was obtained from 30 % H₂O₂ solution diluted to a 100-1000 μ M concentration.

3.2.13. *In vitro* cytotoxicity

In vitro cytotoxicity tests were conducted by the cell attachment and viability of the hydrogels using human dermal fibroblasts (HDF). The cells were cultured in alpha minimum essential medium (α -MEM, Welgene, Korea) containing 10 % fetal bovine serum (Gibco, USA) and 1 % penicillin-streptomycin (Pen strep, Gibco, USA) in the incubator at 37 °C under 5 % CO₂. To observe the aspect of cell attachment, the cells adjusted to a density of 5 x 10⁴ cells/mL were seeded onto the hydrogels on the 4 well culture plate. After culturing for 24 h, the samples were stained with green-fluorescent calcein AM (Thermo scientific, USA) for 30 min to observe the morphology of attached cells using confocal laser scanning microscope (CLSM, LSM710, Carl Zeiss, Germany).

Cell viability was assessed using WST-8 cell viability assay (Quantimax™, Biomax, Korea). The cells were suspended onto the 24 well culture plate at a density of 1×10^4 cells/mL with incubation for 24 h at 37 °C, followed by placing the hydrogels in the solution for 24 h. Afterwards, the cell culture medium was substituted with 10 % WST-8 solution and cultivated for 2 h. The obtained formazan products in the reactant were analyzed with a light absorbance at 450 nm on a microplate reader (EZ read 400, Biochrom, UK). Cell viability was represented as a percentage compared with tissue culture plate.

3.2.14. *In vivo* antibacterial performance

To evaluate the antibacterial performance of HCZ hydrogels, the bacteria infection model under the subcutaneous skin tissue of Balb/c mice was introduced for animal experiments. The dorsal hair of mice was removed and the subcutaneous skin was inoculated with 100 µl of *S.aureus* (OD = 1). After inoculation for 48 h, 100 µl of four kinds of specimen, PBS, HAZ, HCZ 3, HCZ 10, were injected into the infected tissue. After 2 days, the mice were sacrificed for harvesting the treated tissues. For colony formation test, the infected tissues were grinded and diluted to PBS solution. Next, 200 µl of diluted suspension was placed and cultured on the LB agar plates for 24 h at 37 °C. Colony

formation images were procured by the digital camera, and the number of colony formation was counted using Image J software. For the histological analysis, the infected tissues were collected and fixed in paraformaldehyde solution (4%). The paraffin blocks were fabricated and sectioned (4 μ m), followed by obtaining histological images using Hematoxylin and Eosin (H&E, ab245880, Abcam, UK). The abscesses area was calculated using the following equation:

$$\text{Abscesses area (mm}^2\text{)} = \text{long dimension} * \text{short dimension}$$

The bacterial band length (Measured both edges against the center of the abscess) in H&E stained sections (40x magnification) and cellularity in H&E stained sections (400x magnification) were determined for each section using an microscope (BX53, Olympus Corporation, Japan). For peripheral blood profiles of the whole blood samples were collected for each group at the time of sacrifice. An automatic hematology analyzer (XN-1000, SYSMEX, JAPAN) was used to perform the white blood cells counts. C-Reactive Protein (CRP) level, serum isolated from whole blood were performed using enzyme-linked immunosorbent assay kit (ELISA, ab157712, Abcam).

3.2.15. Statistical analysis

All experimental results were statistically represented as the mean \pm standard deviations. The Statistical Package for the Social Sciences (SPSS, IBM, USA) was utilized to analyze the difference between specimens. Normality of the variables was evaluated using one-way analysis of variance (ANOVA) and a Tukey's post-hoc analysis. A p value below 0.05 was considered to be significant in all cases.

3.3. Results and discussion

3.3.1. Synthesis and characterization of HCZ hydrogels

The fabrication process of HA-CA polymers was illustrated in **Figure 3.2A**. First, HA-CA was prepared with EDS/NHS coupling agents. Functionalized catechol from HA-CA was identified by a $^1\text{H-NMR}$ spectrum. A signal at around 2 ppm corresponded to the methyl protons of the N-acetyl group from HA (**Figure 3.2B**) [99]. The peaks between $\delta= 6.7$ ppm and $\delta= 7.0$ ppm corresponded to the characteristic peaks of dopamine, which indicates the proton in ortho and meta coupling position of aromatic ring as shown in **Figure 3.2C** [100]. The conjugation ratio of HA-CA was determined using UV-Vis spectroscopy as depicted in **Figure 3.2D**. To calculate the conjugation ratio of

dopamine on HA, dopamine standard curves were obtained at approximately 280 nm. The concentration of dopamine was 0.256 mM using measured absorbance of HA-CA at approximately 280 nm. Consequently, the degree of conjugated dopamine was 9.9 %. Next, ZnO nanoparticles were synthesized using a precipitation method at room temperature. TEM images revealed that the average diameter of ZnO nanoparticles was 34.1 ± 10.4 nm as described in **Figure 3.3**. Consequently, the solution which mixed HA-CA and ZnO nanoparticles was cured at 50 °C for 24 h to fabricate hydrogels based on catechol-ZnO complexes (HCZ) (**Figure 3.4A**). The phase transition from sol to gel of HCZ was observed as shown in **Figure 3.4B**. After gelation, the color of HCZ hydrogel was changed from gray into black. Elevated temperature above the room temperature was anticipated to accelerate the reaction rate of cross-linking on the surface of ZnO nanoparticles with catechol. In this hydrogel structure, a ZnO nanoparticle acted as a cross-linker via the coordination bond between catechol moiety and the particle. Multivalent coordination bonds of catechol with metal oxide nanoparticles can create the cross-linking system which produce the hydrogel matrix [93]. To identify the characteristics derived from catechol-ZnO complexes, chemically cross-linked HAZ hydrogel was established as another experimental group which was much transparent compared with HCZ hydrogels (**Figure 3.4C**). In **Figure 3.5**, the surface morphology of lyophilized hydrogels was observed using SEM. All

specimens had a porous structure which was an evidence of hydrogel structure synthesis.

XRD diffraction patterns in **Figure 3.6A** exhibited the crystallinity of ZnO nanoparticles and hydrogels with different concentrations of ZnO nanoparticles. The high crystallinity of synthesized ZnO nanoparticles was plainly proved by observing the characteristic peaks of ZnO. In case of HCZ hydrogels, the ZnO related peak intensity was increased along with the contents of ZnO nanoparticles in the hydrogels. **Figure 3.6B** revealed FT-IR spectra of hydrogels for examining the chemical structure according to the cross-linking system. The C-H stretching peak at 2856 cm^{-1} was observed in HAZ hydrogel due to the chemical cross-linker, BDDE. Catechol moieties of HCZ hydrogels were determined by aromatic C=C peaks at 1563 cm^{-1} . The UV-vis absorption spectra of hydrogels were presented in **Figure 3.6C**. The absorbance band of conjugated catechol and ZnO nanoparticles was observed at approximately 280 nm and 360 nm in the hydrogels, respectively. The absorbance peak of ZnO nanoparticles was assigned to the intrinsic band gap energy absorption [101]. In addition, the absorbance increase of HCZ hydrogels was inspected in a range of visible light due to the interfacial charge transfer from coordination geometry formation between catechol and ZnO. In an interface of HA-CA and ZnO nanoparticles, unique interfacial charge transitions could be occurred via

chelating linkage between catechol moiety and ZnO surface [102]. As increasing the concentration of ZnO nanoparticles, the stronger absorption band was determined in the visible light spectrum because of acquiring more bidentate or monodentate bridge structures.

To understand the chemical structure of HCZ hydrogels, high resolution XPS C 1s spectra of ZnO, HA-CA, and HCZ was revealed in **Figure 3.7**. From **Figure 3.7A**, detected carbon peaks in ZnO nanoparticles such as C-C (sp^2) at 284.4 eV and O-C=O at 288.9 eV were related to the adventitious carbon contamination due to the exposure to an ambient environment. C-OH (285.9 eV) and C=O peaks (287.8 eV) was observed in the HA-CA, which results from the functionalization of catechol groups (**Figure 3.7B**). After HA-CA mixed with ZnO nanoparticles which created catechol-ZnO complexes in HCZ hydrogel, the intensity of C-OH and C=O was quite decreased as detailed in **Figure 3.7C**. It indicates that the coordination bonds between catechol and ZnO nanoparticles were successfully created, which contributed to the gelation of HCZ hydrogel.

The contents of ZnO nanoparticles affected the rheological behavior of HCZ hydrogel as described in **Figure 3.8A**. The storage modulus was obtained using a frequency sweep mode to illustrate the mechanical stiffness. The storage modulus at certain frequency (1 rad/s) was substantially increased

from 108.1 ± 144.5 to 290 ± 916.0 Pa as increasing the incorporation of ZnO nanoparticles from 3 to 10 wt% in HCZ hydrogels. It revealed that the incorporation of more ZnO nanoparticles was increased the cross-link density due to the participation of ZnO nanoparticles as a cross-linker. HAZ hydrogel showed 173.4 ± 30.4 Pa at 1 rad/s frequency which was similar value with HCZ hydrogels.

Swelling behavior of HCZ and HAZ hydrogels was dependent on the concentration and type of cross-linker as shown in **Figure 3.8B**. The swelling ratio of HCZ hydrogels was decreased from 106.7 ± 4.7 to 91.7 ± 2.2 at 72 h incubation as the amounts of ZnO nanoparticles increased. High concentration of ZnO nanoparticles act to increase the cross-linking density via providing more cross-linking sites. Surprisingly, HAZ showed lower swelling ratio compared with HCZ hydrogels. It suggests that the coordination bond mediated cross-linked hydrogels had a higher swelling ratio than that of the chemically cross-linked hydrogel.

In vitro degradation behavior was characterized by a hyaluronidase which was a specific enzyme to degrade the HA as shown in **Figure 3.8C**. Degradation of hydrogels was determined by measuring the remaining weight at the certain incubating time period in the hyaluronidase solution. The enzymatic degradation rate of HAZ hydrogel was considerably faster than HCZ

hydrogels. After 24 h culturing in the enzyme solution at 37 °C, HAZ was fully degraded, whereas the remaining weight of HCZ 3,5, and 10 was 47.4 ± 1.8 , 73.8 ± 3.2 , and 79.7 ± 4.6 %, respectively. This result suggested that the catechol-ZnO coordination complex structure effectively resisted the enzymatic degradation compared with the chemically cross-linked structure. Catechol-ZnO coordination complexes created multiple cross-linking points on the ZnO surface, which resulted in a delay of degradation rate. As increasing the concentration of ZnO nanoparticles in HCZ hydrogels, the remained weight was increased due to the obtaining more cross-linking points. Therefore, it is expected that catechol-ZnO coordination complexes could not only enhance their structure stability of HCZ hydrogels, but induce long-term therapeutic action under the enzymatic degradation.

Tissue adhesive strength of hydrogels was evaluated from the recorded maximum shear stress during the lab shear test as described in **Figure 3.8D**. To compare the adhesive strength of hydrogel itself, fabricated hydrogels were placed on the overlapping surface of porcine skins. The tissue adhesive strength of HCZ hydrogels (0.87 ± 0.13 kPa for HCZ 3, 0.78 ± 0.17 kPa for HCZ 5, and 0.99 ± 0.23 kPa for HCZ 10) was considerably higher than that of HAZ hydrogel (0.26 ± 0.1 kPa). The disparity of tissue adhesive strength between HCZ and HAZ hydrogels was relevant with the different cross-linking mechanism. The catechol moiety from HCZ hydrogels has a tissue adhesive

capability by means of the versatile bonding with the surface including hydrogen bonding. The concentration of functionalized catechol groups contributed to the tissue adhesive strength, which resulted in the similar figures between HCZ hydrogels regardless the amounts of ZnO nanoparticles.

3.3.2. Measurement of enhanced ROS generation

To inspect the free radical formation corresponding to the HCZ hydrogels, the EPR spectra of ZnO, HAZ, and HCZ was displayed in **Figure 3.9A**. The two sharp signals were detected at a g value of 2.0037 and 1.96 in all specimen, which were assigned to radical species generated from the catechol-ZnO complexes and singly ionized oxygen vacancies of ZnO nanoparticles respectively [103, 104]. The graph shape of HAZ was similar with ZnO, which suggests that HA cannot support to generate more radicals after mixing with ZnO nanoparticles. However, the signal intensity of HCZ was extensively intense in both recognized peaks compared with other specimens. It could represent that free radical generation was significantly increased during the coordination geometry formation of catechol-ZnO nanoparticles, which was attributed to o-semiquinone radicals and electron transfer from the oxidation of catechol [105]. Moreover, the catechol-ZnO coordination complex also triggered to increase the intensity of g value of 1.96 which was related to

unpaired electron traps on oxygen vacancy defects [103].

H₂O₂ concentration in the solution after treating the hydrogels was measured at each time interval as detailed in **Figure 3.9B**. The colorimetric method was conducted to clarify H₂O₂ concentration, which measured the absorbance after the color change. The HAZ hydrogel produced few amounts of H₂O₂, while HCZ hydrogels could supply lots of H₂O₂ during the reaction with solution. It indicated that generated radicals from catechol-ZnO coordination complex converts water molecules into H₂O₂ species.

To further verify the oxidative stress by ROS released from HCZ hydrogels, GSH depletion ability of hydrogels was investigated. GSH is capable of protecting various cellular components by neutralizing ROS as oxidizing into glutathione disulfide (GSSG) [106]. Depletion of GSH was quantitatively investigated with ellman's assay for detecting the amount of GSH after interacting with HCZ hydrogels. Control with only GSH and HAZ hydrogel in GSH solution showed no color change after 3 h immersion, whereas the color became gradually transparent in the presence of HCZ hydrogels (**Figure 3.9C**). Loss of GSH was calculated using the absorbance difference after exposing to the hydrogels as shown in **Figure 3.9D**. HCZ hydrogels revealed notably higher GSH oxidation ability (81.5 % ± 4.0 % for HCZ 3, 89.0 % ± 0.5 % for HCZ 5, 90.9 % ± 1.2 % for HCZ 10) than that of HAZ

hydrogel ($7.6 \% \pm 6.2 \%$). It denoted that ROS generation was crucially amplified by the formation of catechol-ZnO complexes in HCZ hydrogels.

These results strongly supported that HCZ hydrogels produce lots of ROS derived from the catechol-ZnO complex structure. We propose that the oxidation of catechol is catalyzed by ZnO nanoparticles in the process of catechol-ZnO complex formation, which induces the electron transfer that converts from O_2 to O_2^{\bullet} and H_2O_2 . Furthermore, *o*-semiquinone radicals generated from the catechol oxidation could also affect to produce additional ROS.

3.3.3. *In vitro* cytocompatibility and antibacterial performance

In vitro cytotoxicity of the hydrogels was evaluated using fluorescence imaging and WST-8 assay which matched with the cell viability. **Figure 3.10A** represented typical CLSM images of cell attachment on the hydrogels after 24 h culturing. Few HDF cells were attached on the surface of HAZ hydrogel, whereas a plenty of cells were firmly adhered for HCZ hydrogels. It suggests that catechol groups in HCZ hydrogels enhanced the initial cell attachment ability. In addition, no dead cells were observed in the hydrogels except HCZ 10. HCZ 10 showed relatively many dead cells compared with other hydrogels.

The cell viability of the hydrogels was displayed in **Figure 3.10B**. To assess the cytotoxicity from the hydrogels, the samples were immersed in the media including a monolayer of cells for 24 h. Although no cytotoxicity was observed in HAZ, HCZ 3, and HCZ 5, cell viability of HCZ 10 was slightly decreased due to the high density of ZnO nanoparticles.

The antibacterial performance of HCZ hydrogels was examined against two different bacterial strains, *E.coli* and *S.aureus*, which are representative of typical infection bacteria. As shown in **Figure 3.11A**, disk diffusion test was conducted to identify the antibacterial efficacy of the hydrogels. No inhibition zone was observed in HAZ hydrogel, while distinct inhibition zones was produced in HCZ 3, 5, and 10 for both bacterial strains. The bactericidal efficacy was also revealed by measuring the OD value at 595 nm after culturing 24 h for both strains according to **Figure 3.11B**. The OD value indicated the concentration of bacteria in solution. The HAZ hydrogel showed weak antibacterial performance in *S. aureus* owing to the inherent antibacterial characteristics of ZnO nanoparticles. The OD of both bacteria was remarkably decreased after treating the HCZ hydrogels compared with HAZ hydrogel. Although the amount of ZnO nanoparticles in HAZ and HCZ 3 was identical, HCZ 3 showed excellent antibacterial property. It was consistent with the result of disk diffusion test which corroborated the antibacterial property of

HCZ hydrogels. In **Figure 3.11C**, enhanced ROS generation was also proved by the detection of intracellular ROS in *S.aureus*. The level of intracellular ROS was defined with the relative concentration of fluorescent 2',7'-dichlorodihydrofluorescein (DCF). No significant increase of DCF intensity was observed in HAZ compared with control group. However, the fluorescence intensity of HCZ 3 was remarkably enhanced though HCZ 3 and HAZ contained the same concentration of ZnO nanoparticles. It demonstrated that the amount of intracellular ROS was elevated by catechol-ZnO complexes, not ZnO nanoparticles itself. In addition, as increasing the concentration of ZnO nanoparticles in the hydrogel, intracellular ROS generation was boosted because of more catechol-ZnO complex formation. Hence, the morphology of bacteria exposed to hydrogels was observed to unveil the antibacterial activity of HCZ hydrogels (**Figure 3.12**). No deformation of bacteria structure was recognized in case of HAZ hydrogel, while both bacteria membrane was ruptured after culturing on HCZ hydrogels. These results were attributed to the high concentration of ROS release from HCZ hydrogels which is the major factor for killing the two bacterial strains effectively. Excessive ROS generation produced the enormous oxidative stress which induces membrane disruption and DNA damage of bacteria cells [107].

3.3.4. *In vivo* antibacterial performance of HCZ hydrogels

To further investigate the antibacterial performance of HCZ hydrogels, *in vivo* bacterial infection model was constructed using *S.aureus*. The subcutaneous skin tissues were inoculated with *S.aureus* for 2 days, followed by an injection of PBS, HAZ, HCZ 3, and HCZ 10 hydrogels into the infected tissues as described in **Figure 3.13A**. For the injection of hydrogels, they were crushed through a homogenizer. After treating with hydrogels for 2 days, the mice were sacrificed and the infected sites were harvested. The antibacterial performance of HCZ hydrogels from *in vivo* animal experiments was evaluated with colony formation test (**Figure 3.13B**). Treated tissues with PBS solution was established to the negative control. In case of HAZ hydrogel, the number of colony was not decreased compared with the control, which indicates less effective antibacterial properties in spite of containing ZnO nanoparticles. However, the number of bacteria colony was drastically decreased about 4 times by treating with the HCZ 3 and HCZ 10 hydrogels. Especially, the HCZ 3 hydrogel revealed excellent antibacterial performance despite the presence of the same concentration of ZnO nanoparticles as the HAZ hydrogel. It suggests that catechol-ZnO complexes support to increase the antibacterial capability rather than the ZnO nanoparticle itself. In **Figure. 3.14A**, H&E histological sections images of each specimens revealed that plenty of inflammatory cells

were obviously observed in the infected sites. Abscess area, bacterial band length, and cellularity were calculated from the H&E histological images to determine the antibacterial performance quantitatively. The abscess area and bacterial band length of HCZ 3 and HCZ 10 was reduced compared with control and HAZ groups, especially HCZ 10 significantly diminished the abscess area (**Figure. 3.14B-C**). The bacteria cellularity showed a similar tendency with other quantitative figures, which indicated HCZ 3 and HCZ 10 confirmly decreased the abundant inflammatory cells as detailed in **Figure. 3.14D**. Since White Blood Cell (WBC) and neutrophil counts are generally known as sensitive and reliable indicators of inflammatory activity [108], additional *in vivo* hematological analysis was performed. At the time of sacrifice, we conducted hemanalysis for analysis of peripheral blood profiles. In **Figure. 3.15A**, Differential count of WBC as the proportion of cell component showed significantly low expressed in the proportion of neutrophils in HCZ 10. The absolute WBC and neutrophils counts were significantly decreased in the HCZ 10 (**Figure. 3.15B-C**). In addition, we measured serum C-Reactive Protein (CRP) that is known as an maker of acute protein that is highly expressed in inflammation and tissue damage [109]. Serum CRP levels in infected-mice were observed to be slightly lower in case of HCZ 3, and significantly lower in the regulated HCZ 10 groups compared to the control groups (**Figure. 3.15D**). These results demonstrated that HCZ hydrogels showed effective antibacterial

properties in the histological and hematological analysis. Furthermore, the antibacterial performance was substantially improved as an increase of ZnO nanoparticle concentration in HCZ hydrogels.

3.4. Conclusions

In summary, we have successfully developed a hyaluronic acid hydrogel platform via catechol-ZnO complexes for antibacterial therapy. The hydrogel system was fabricated via the reversible coordination cross-linking bonds between catechol moieties and ZnO nanoparticles. This hydrogel showed an excellent tissue adhesive property due to the presence of functionalized catechol groups in the hydrogel matrix. By taking advantage of ROS generation during the catechol-ZnO complex formation, this hydrogel platform revealed enhanced ROS generation as well as outstanding antibacterial performance against both *E.coli* and *S.aureus*. In addition, a mouse full-thickness *S.aureus* infection model also demonstrated HCZ hydrogels had remarkable potentials to eradicate the bacteria. This work represents a new approach to design the ROS self-generating hydrogel platform for enhanced antibacterial therapy.

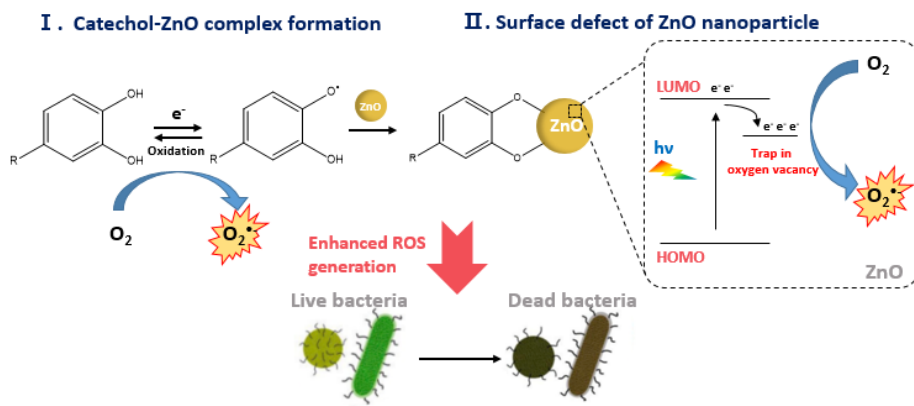


Figure 3.1. Schematic illustration about the mechanism of enhanced ROS generation through catechol-ZnO complexes

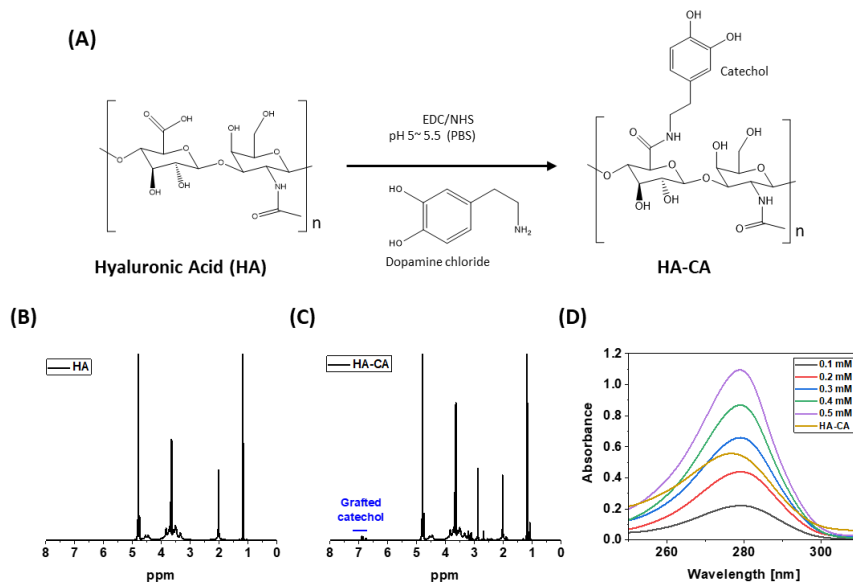


Figure 3.2. Schematic diagrams of (A) synthesis of HA-CA polymer, $^1\text{H-NMR}$ spectra of (B) HA and (C) HA-CA polymer. (D) Absorbance spectra of dopamine solution with different concentrations and HA-CA

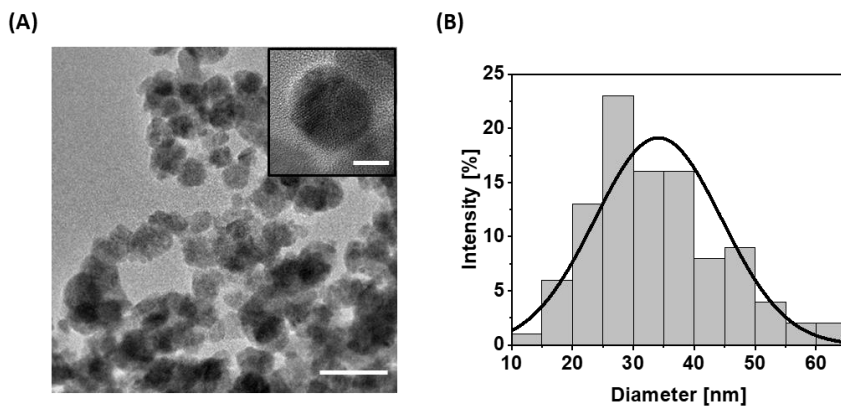


Figure 3.3. (A) TEM images of ZnO nanoparticles in low (Scale bar = 100 nm) and high resolution (Inset, scale bar =10 nm). (b) Size distribution of ZnO nanoparticles

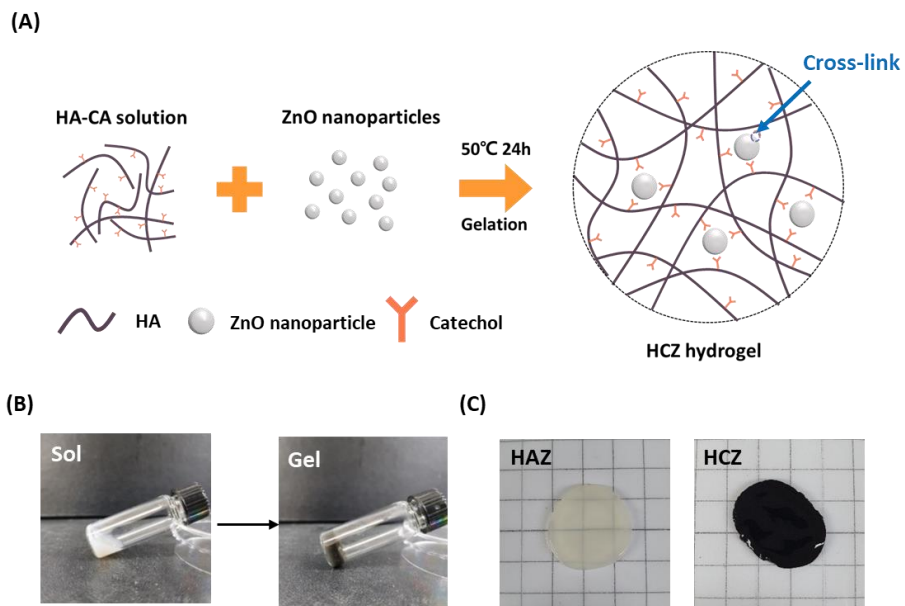


Figure 3.4. (A) Schematic illustrations of the preparation of HCZ hydrogel. (B) Phase transition of HCZ hydrogel, and (C) optic images of HAZ (left) and HCZ hydrogel (right)

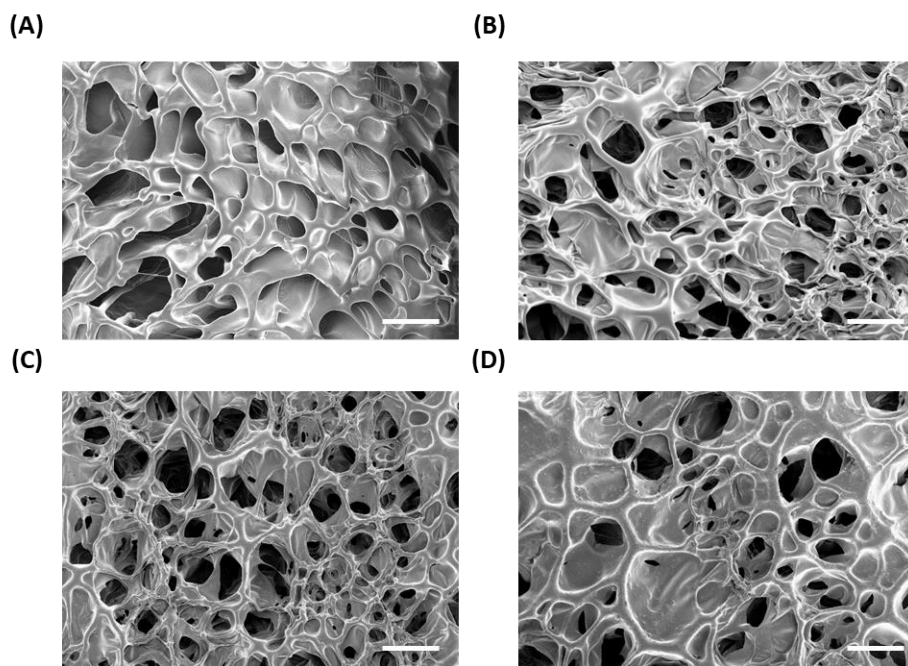


Figure 3.5. SEM images of lyophilized (A) HAZ, (B) HCZ 3, (C) HCZ 5, and (D) HCZ 10 hydrogels (Scale bar =40 μm)

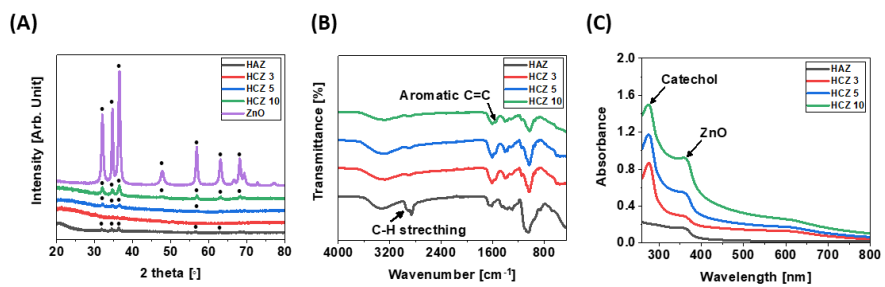


Figure 3.6. (A) XRD patterns, (B) FT-IR spectra, and (C) UV-vis absorbance spectra of HAZ and HCZ hydrogels

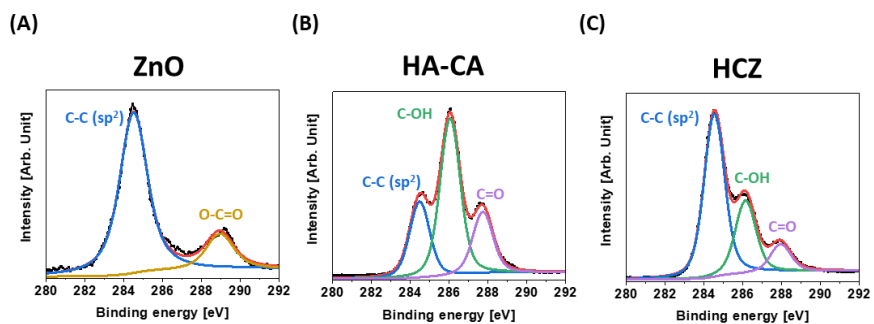


Figure 3.7. High resolution XPS spectra of the carbon region (C 1s) for (A) the ZnO nanoparticles, (B) HA-CA, and (C) HCZ hydrogel respectively.

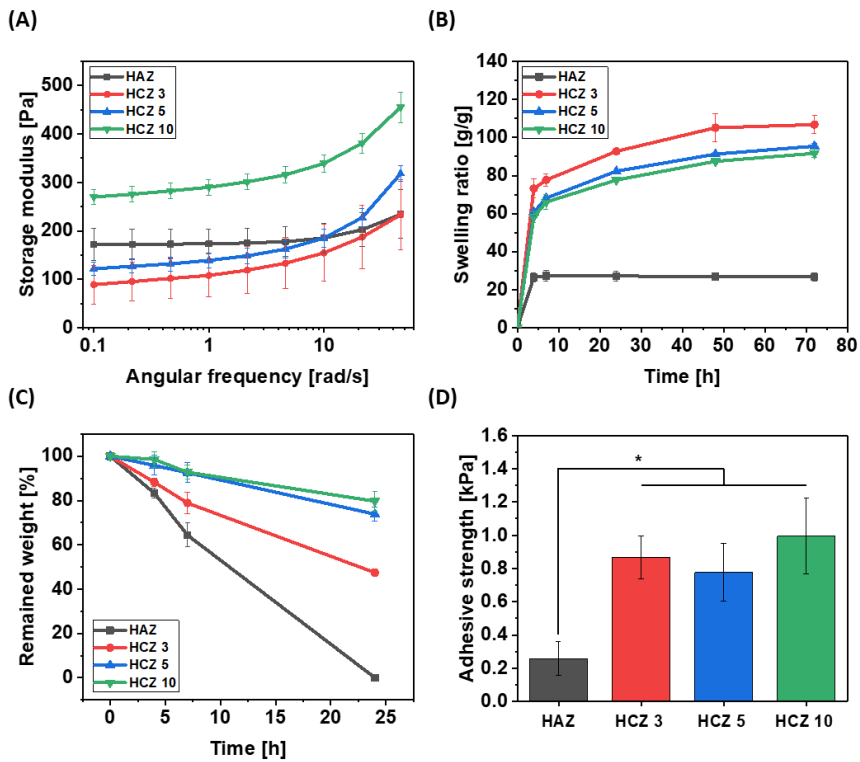


Figure 3.8. Characterization of HCZ hydrogels: (A) Rheological behavior represented from storage modulus for a frequency sweep mode. (B) Swelling ratio of the hydrogels for different time periods, 4, 7, 24, 48, 72 h. (C) In vitro enzymatic degradation behavior of the hydrogels in the presence of hyaluronidase. (D) Tissue adhesive strength of the hydrogels calculated from lab shear strength. (*: $p < 0.05$)

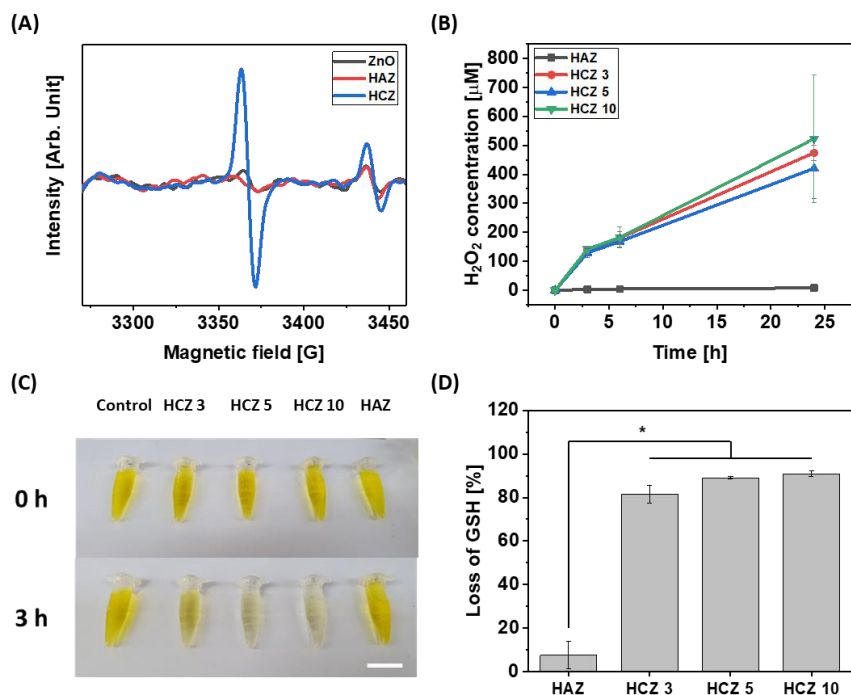


Figure 3.9. (A) EPR spectrum of ZnO, HAZ, and HCZ. (B) H₂O₂ concentration generated from HAZ and HCZ hydrogels with different ZnO amounts. (C) Optic images of color change of GSH after the hydrogel immersion at 37 °C for 0 h and 3 h respectively. (Scale bar: 2 cm) (D) Loss of GSH level after treating with hydrogels for 3 h.

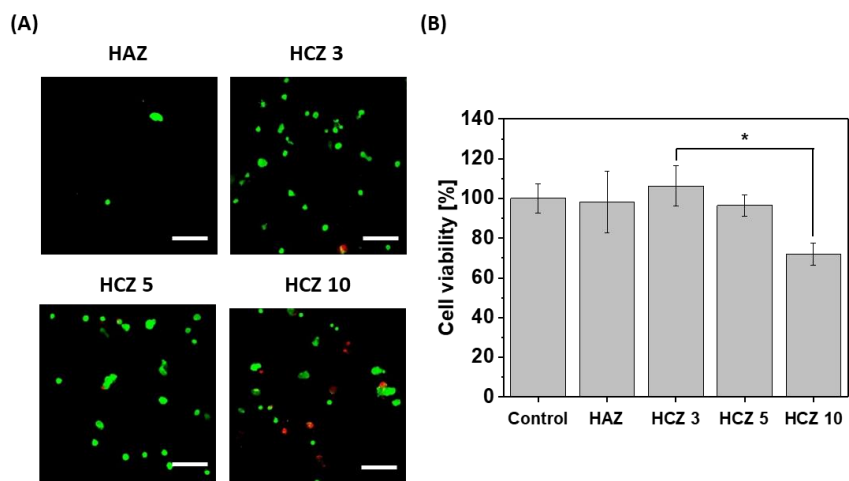


Figure 3.10. (A) CLSM images of cultured HDF cells attached on HAZ and HCZ hydrogels. (B) Relatively cell viability evaluation of HAZ and HCZ hydrogels after 24 h culturing in HDF cells. (Scale bar: 200 μm , *: $p < 0.05$)

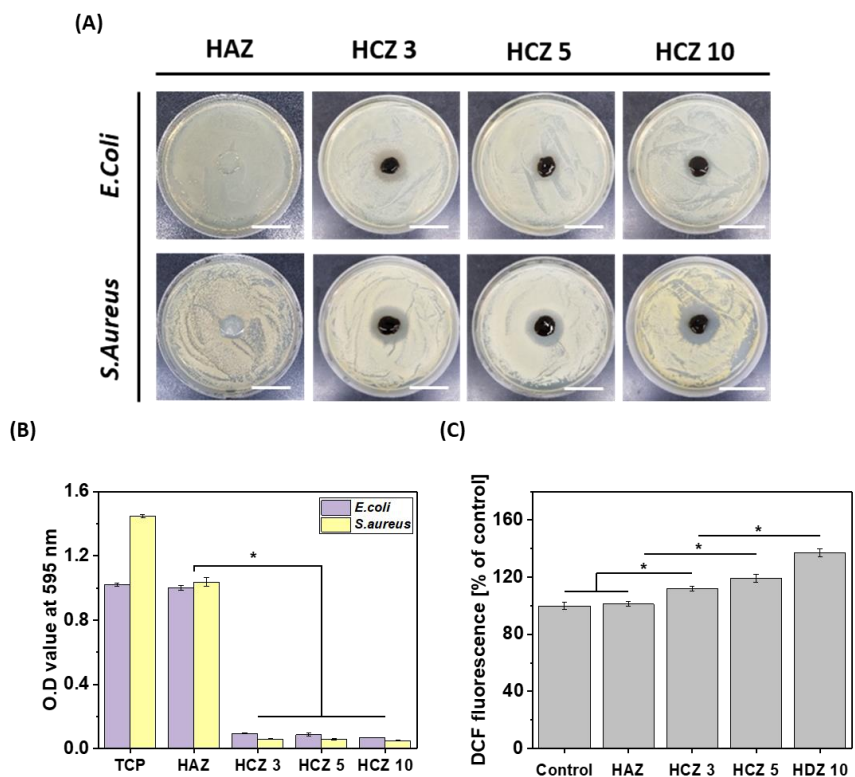


Figure 3.11. (A) Disk diffusion test images against *E. coli* and *S. aureus* of HAZ and HCZ hydrogels. (Scale bar: 20 mm) (B) Bactericidal efficacy of hydrogels against both bacteria strain after 24 h incubation. (*: $p < 0.05$) (C) The level of intracellular ROS generation in *S. aureus* after treatment with HAZ and HCZ hydrogels. (*: $p < 0.05$)

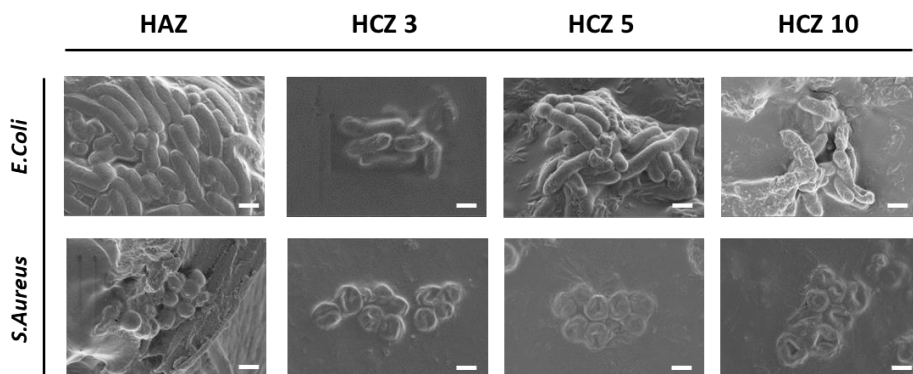


Figure 3.12. Morphology of *E.coli* and *S.aureus* attached on the surface of the hydrogels. (Scale bar: 1 μ m)

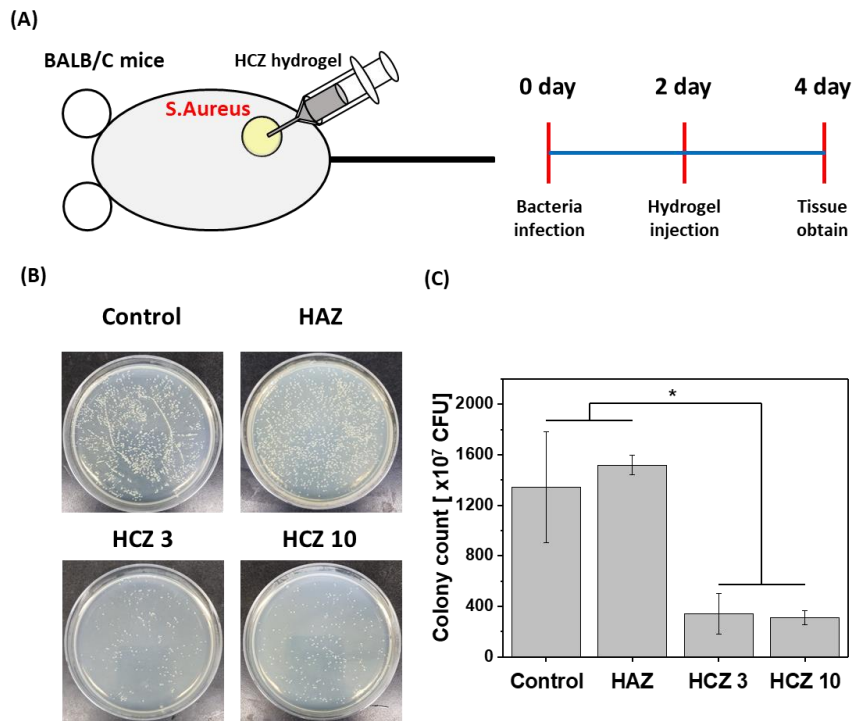


Figure 3.13. (A) Schematic experimental designs of *in vivo* bacterial infection model in the subcutaneous skin of mouse. (B) Colony formation after treating with the hydrogels for 2 days, and (C) calculated count of colonies for each specimen. (*: $p < 0.05$)

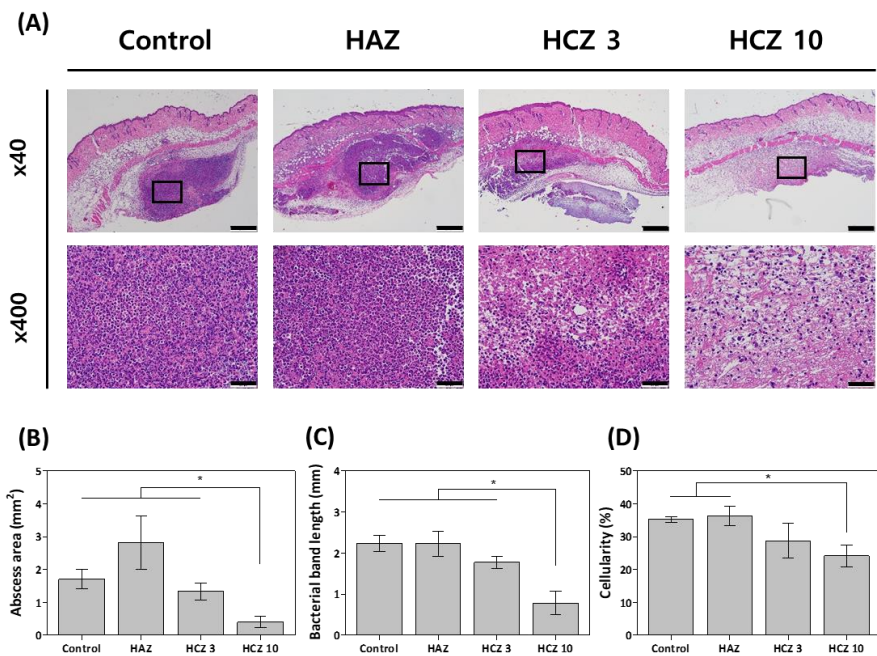


Figure 3.14. (A) Representative histological sections images of *S. aureus*-infected skin lesions with H&E stain. (Original magnification: x40-Scale bar=500 μ m, Original magnification: x400-Scale bar= 50 μ m) (B) Mean abscess area (mm^2), (C) mean bacterial band length (mm), and (D) density of cellularity (%) from H&E stain sections. (*: $p < 0.05$)

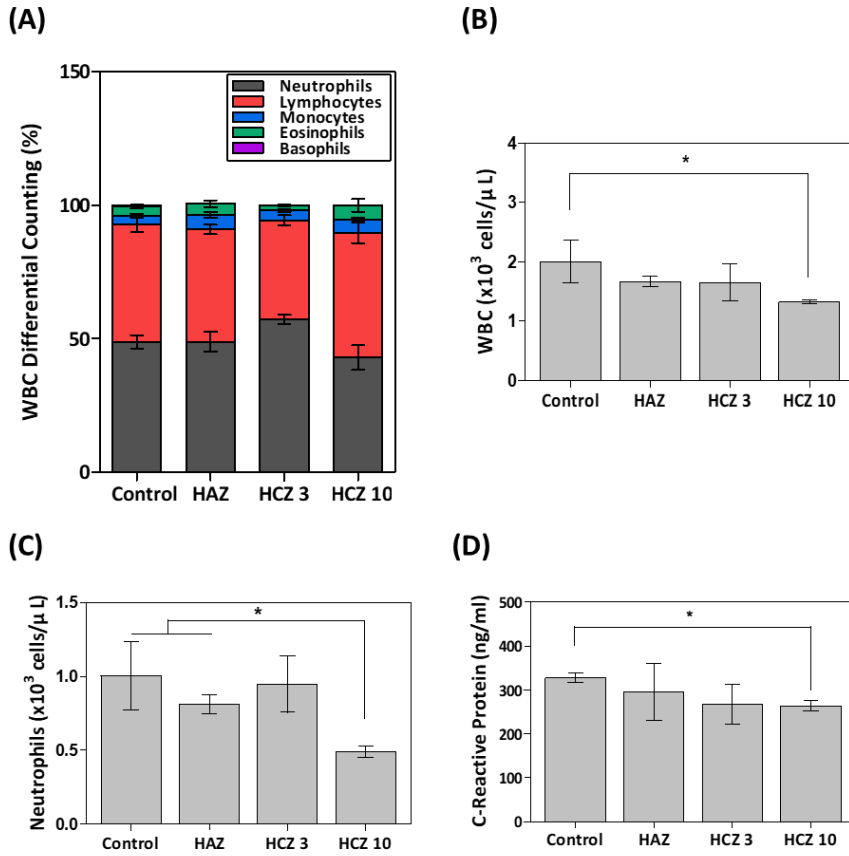


Figure 3.15. Analysis of peripheral blood profiles in control, HAZ, HCZ3, and HCZ 10 mice at the time of sacrifice: (A) Proportion of neutrophils, lymphocytes, monocytes, eosinophils, and basophils in whole blood samples. (B) Absolute WBC counts, (C) Neutrophils counts, and (D) c-reactive protein (CRP) level. (*: $p < 0.05$)

Chapter 4.
Conclusions

4.1. Conclusions

This thesis aimed to improve mechanical and biological functions of HA hydrogels through the incorporation of nanoparticles including SiO₂ and ZnO nanoparticles for biomedical applications. For adopting HA hydrogels to the various parts of tissue engineering, enhanced mechanical properties and biological functions were essential.

In Chapter 2, we successfully developed HA-SiO₂ nanocomposite hydrogel coatings with enhanced mechanical stability and biolubrication performance using EPD and *in situ* sol-gel process. *In situ* sol-gel method enabled to create the stable HA-SiO₂ nanocomposite suspension, which is favorable to fabricate the coatings by EPD technique. The incorporated SiO₂ nanoparticles were homogeneously distributed in the HA. HA-SiO₂ nanocomposite coatings enhanced the mechanical stability because of mechanical interlocking and enrichment of polar groups. In addition, biolubrication performance of the coatings was also investigated with a customized friction model using a PDMS substrate. HA-SiO₂ nanocomposite coatings showed lower CoF value compared with HA coating, which confirmed the enhanced biolubrication performance. These findings suggest that the incorporation of SiO₂ nanoparticles in HA hydrogel coating enhanced not only the mechanical stability, but also biolubrication performance.

In Chapter 3, catechol-ZnO complexes based HA hydrogels were

fabricated with enhanced the antibacterial property. Catechol moieties were introduced for compensating the disadvantages of ZnO nanoparticles as an antibacterial agents. Coordination bonds between catechol groups and ZnO nanoparticles were attributed to create the cross-linking network in the polymer matrix. Hence, the formation of catechol-ZnO complexes via coordination bonds confirmly increased ROS generation. The different characteristics of HCZ hydrogels arised from catechol-ZnO complex were identified as comparing with chemically cross-linked hydrogel system, HAZ hydrogel. Tissue adhesive strength of HCZ hydrogels was higher than the HAZ hydrogel due to the presence of catechol moieties conjugated with HA. HCZ hydrogels revealed the increase of ROS generation via the electron transfer during the formation of catechol-ZnO complxes. *In vitro* cytocompatibility test was implemented to analyze the biological affinities of HCZ hydrogels. *In vitro* antibacterial test represented HCZ hydrogels showed excellent antibacterial performance rather because of enhanced ROS releasing from the hydrogels. Moreover, *in vivo* animal experiments also proved that HCZ hydrogels considerably reduced the number of S.aureus in the subcutaneous tissue, which indicates the strong capability of them to eradicate the bacteria. These findings indicate that HCZ hydrogels deliver large amounts of ROS to the bacteria, which results in a promising antibacterial therapeutics.

This study suggests the great potential of HA based nanocomposite

hydrogel via the incorporation of numerous nanoparticles for biomedical applications. This system not only enhances the mechanical properties, but also establishes the crucial functionality which meets the purpose of applications. Based on this research, further researches could be reported in terms of HA nanocomposite hydrogels using other nanomaterials for the different purpose.

References

- [1] N. Almouemen, H.M. Kelly, C. O'Leary, Tissue Engineering: Understanding the Role of Biomaterials and Biophysical Forces on Cell Functionality Through Computational and Structural Biotechnology Analytical Methods, *Comput Struct Biotechnol J*, 17 (2019) 591-598.
- [2] M. Asadian, K.V. Chan, M. Norouzi, S. Grande, P. Cools, R. Morent, N. De Geyter, Fabrication and Plasma Modification of Nanofibrous Tissue Engineering Scaffolds, *Nanomaterials (Basel)*, 10 (2020).
- [3] B. Dhandayuthapani, Y. Yoshida, T. Maekawa, D.S. Kumar, Polymeric Scaffolds in Tissue Engineering Application: A Review, *International Journal of Polymer Science*, 2011 (2011) 1-19.
- [4] J.J. Elsner, A. Kraitzer, O. Grinberg, M. Zilberman, Highly porous drug-eluting structures: from wound dressings to stents and scaffolds for tissue regeneration, *Biomatter*, 2 (2012) 239-270.
- [5] J. Tang, J. Guo, Z. Li, C. Yang, D. Xie, J. Chen, S. Li, S. Li, G.B. Kim, X. Bai, Z. Zhang, J. Yang, Fast degradable citrate-based bone scaffold promotes spinal fusion, *J Mater Chem B*, 3 (2015) 5569-5576.

- [6] O. Okolie, I. Stachurek, B. Kandasubramanian, J. Njuguna, 3D Printing for Hip Implant Applications: A Review, *Polymers (Basel)*, 12 (2020).
- [7] C.T. Johnson, A.J. Garcia, Scaffold-based anti-infection strategies in bone repair, *Ann Biomed Eng*, 43 (2015) 515-528.
- [8] S.M. McNary, K.A. Athanasiou, A.H. Reddi, Engineering lubrication in articular cartilage, *Tissue Eng Part B Rev*, 18 (2012) 88-100.
- [9] C.D. Spicer, Hydrogel scaffolds for tissue engineering: the importance of polymer choice, *Polymer Chemistry*, 11 (2020) 184-219.
- [10] I.M. El-Sherbiny, M.H. Yacoub, Hydrogel scaffolds for tissue engineering: Progress and challenges, *Glob Cardiol Sci Pract*, 2013 (2013) 316-342.
- [11] M.A. Radwan, O.H. Al-Sweasy, H.A. Elazab, Preparation of Hydrogel Based on Acryl Amide and Investigation of Different Factors Affecting Rate and Amount of Absorbed Water, *Agricultural Sciences*, 08 (2017) 161-170.
- [12] S. Naahidi, M. Jafari, M. Logan, Y. Wang, Y. Yuan, H. Bae, B. Dixon, P.

Chen, Biocompatibility of hydrogel-based scaffolds for tissue engineering applications, *Biotechnol Adv*, 35 (2017) 530-544.

[13] Z. Bao, C. Xian, Q. Yuan, G. Liu, J. Wu, Natural Polymer-Based Hydrogels with Enhanced Mechanical Performances: Preparation, Structure, and Property, *Adv Healthc Mater*, 8 (2019) e1900670.

[14] S. Jiang, S. Liu, W. Feng, PVA hydrogel properties for biomedical application, *J Mech Behav Biomed Mater*, 4 (2011) 1228-1233.

[15] W. Tanan, J. Panichpakdee, S. Saengsuwan, Novel biodegradable hydrogel based on natural polymers: Synthesis, characterization, swelling/reswelling and biodegradability, *European Polymer Journal*, 112 (2019) 678-687.

[16] D.A. Gyles, L.D. Castro, J.O.C. Silva, R.M. Ribeiro-Costa, A review of the designs and prominent biomedical advances of natural and synthetic hydrogel formulations, *European Polymer Journal*, 88 (2017) 373-392.

[17] K.T. Dicker, L.A. Gurski, S. Pradhan-Bhatt, R.L. Witt, M.C. Farach-Carson, X. Jia, Hyaluronan: a simple polysaccharide with diverse biological functions, *Acta Biomater*, 10 (2014) 1558-1570.

- [18] H. Park, B. Choi, J. Hu, M. Lee, Injectable chitosan hyaluronic acid hydrogels for cartilage tissue engineering, *Acta Biomater*, 9 (2013) 4779-4786.
- [19] J.A. Burdick, G.D. Prestwich, Hyaluronic acid hydrogels for biomedical applications, *Adv Mater*, 23 (2011) H41-56.
- [20] S. Khunmanee, Y. Jeong, H. Park, Crosslinking method of hyaluronic-based hydrogel for biomedical applications, *J Tissue Eng*, 8 (2017) 2041731417726464.
- [21] H. Li, Z. Qi, S. Zheng, Y. Chang, W. Kong, C. Fu, Z. Yu, X. Yang, S. Pan, The Application of Hyaluronic Acid-Based Hydrogels in Bone and Cartilage Tissue Engineering, *Advances in Materials Science and Engineering*, 2019 (2019) 1-12.
- [22] S. Suri, C.E. Schmidt, Photopatterned collagen-hyaluronic acid interpenetrating polymer network hydrogels, *Acta Biomater*, 5 (2009) 2385-2397.
- [23] W. Xu, J. Qian, Y. Zhang, A. Suo, N. Cui, J. Wang, Y. Yao, H. Wang, A

double-network poly(N-varepsilon-acryloyl L-lysine)/hyaluronic acid hydrogel as a mimic of the breast tumor microenvironment, *Acta Biomater*, 33 (2016) 131-141.

[24] Y. Qiao, S. Xu, T. Zhu, N. Tang, X. Bai, C. Zheng, Preparation of printable double-network hydrogels with rapid self-healing and high elasticity based on hyaluronic acid for controlled drug release, *Polymer*, 186 (2020).

[25] L. Weng, A. Gouldstone, Y. Wu, W. Chen, Mechanically strong double network photocrosslinked hydrogels from N,N-dimethylacrylamide and glycidyl methacrylated hyaluronan, *Biomaterials*, 29 (2008) 2153-2163.

[26] S.H. Jeong, Y.H. Koh, S.W. Kim, J.U. Park, H.E. Kim, J. Song, Strong and Biostable Hyaluronic Acid-Calcium Phosphate Nanocomposite Hydrogel via in Situ Precipitation Process, *Biomacromolecules*, 17 (2016) 841-851.

[27] A. GhavamiNejad, C.H. Park, C.S. Kim, In Situ Synthesis of Antimicrobial Silver Nanoparticles within Antifouling Zwitterionic Hydrogels by Catecholic Redox Chemistry for Wound Healing Application, *Biomacromolecules*, 17 (2016) 1213-1223.

- [28] Z. Tai, J. Yang, Y. Qi, X. Yan, Q. Xue, Synthesis of a graphene oxide–polyacrylic acid nanocomposite hydrogel and its swelling and electroresponsive properties, *RSC Advances*, 3 (2013).
- [29] A.A. Adewunmi, S. Ismail, A.S. Sultan, Carbon Nanotubes (CNTs) Nanocomposite Hydrogels Developed for Various Applications: A Critical Review, *Journal of Inorganic and Organometallic Polymers and Materials*, 26 (2016) 717-737.
- [30] A.K. Gaharwar, N.A. Peppas, A. Khademhosseini, Nanocomposite hydrogels for biomedical applications, *Biotechnol Bioeng*, 111 (2014) 441-453.
- [31] J. Yang, C.R. Han, J.F. Duan, F. Xu, R.C. Sun, In situ grafting silica nanoparticles reinforced nanocomposite hydrogels, *Nanoscale*, 5 (2013) 10858-10863.
- [32] H. Sun, J. Zhou, Z. Huang, L. Qu, N. Lin, C. Liang, R. Dai, L. Tang, F. Tian, Carbon nanotube-incorporated collagen hydrogels improve cell alignment and the performance of cardiac constructs, *Int J Nanomedicine*, 12 (2017) 3109-3120.

- [33] O. Catanzano, V. D'Esposito, G. Pulcrano, S. Maiolino, M.R. Ambrosio, M. Esposito, A. Miro, F. Ungaro, P. Formisano, M.R. Catania, F. Quaglia, Ultrasmall silver nanoparticles loaded in alginate–hyaluronic acid hybrid hydrogels for treating infected wounds, *International Journal of Polymeric Materials and Polymeric Biomaterials*, 66 (2017) 626-634.
- [34] L. Liu, Y. Liu, J. Li, G. Du, J. Chen, Microbial production of hyaluronic acid: current state, challenges, and perspectives, *Microbial cell factories*, 10 (2011) 1-9.
- [35] A. Fallacara, E. Baldini, S. Manfredini, S. Vertuani, *Hyaluronic Acid in the Third Millennium*, *Polymers (Basel)*, 10 (2018).
- [36] P. Le Thi, Y. Lee, T.T. Hoang Thi, K.M. Park, K.D. Park, Catechol-rich gelatin hydrogels in situ hybridizations with silver nanoparticle for enhanced antibacterial activity, *Mater Sci Eng C Mater Biol Appl*, 92 (2018) 52-60.
- [37] L. Xu, C. Wang, Y. Cui, A. Li, Y. Qiao, D. Qiu, Conjoined-network rendered stiff and tough hydrogels from biogenic molecules, *Science advances*, 5 (2019) eaau3442.

[38] G. Reina, J.M. Gonzalez-Dominguez, A. Criado, E. Vazquez, A. Bianco, M. Prato, Promises, facts and challenges for graphene in biomedical applications, *Chem Soc Rev*, 46 (2017) 4400-4416.

[39] H.-Y. Lee, J. Kim, C.-H. Hwang, H.-E. Kim, S.-H. Jeong, Strategy for Preparing Mechanically Strong Hyaluronic Acid-Silica Nanohybrid Hydrogels via In Situ Sol-Gel Process, *Macromolecular Materials and Engineering*, 303 (2018).

[40] R.I. Mehta, R.I. Mehta, O.E. Solis, R. Jahan, N. Salamon, J.M. Tobis, W.H. Yong, H.V. Vinters, M.C. Fishbein, Hydrophilic polymer emboli: an under-recognized iatrogenic cause of ischemia and infarct, *Mod Pathol*, 23 (2010) 921-930.

[41] T. Hasebe, Y. Matsuoka, H. Kodama, T. Saito, S. Yohena, A. Kamijo, N. Shiraga, M. Higuchi, S. Kuribayashi, K. Takahashi, T. Suzuki, Lubrication performance of diamond-like carbon and fluorinated diamond-like carbon coatings for intravascular guidewires, *Diamond and Related Materials*, 15 (2006) 129-132.

[42] L. Dai, H.A. StJohn, J. Bi, P. Zientek, R.C. Chatelier, H.J.J.S. Griesser,

I.A.A.I.J.d.t.t. development, i. application of techniques for the analysis of surfaces, t. films, Biomedical coatings by the covalent immobilization of polysaccharides onto gas-plasma-activated polymer surfaces, 29 (2000) 46-55.

[43] J.H. Bongaerts, J.J. Cooper-White, J.R.J.B. Stokes, Low biofouling chitosan-hyaluronic acid multilayers with ultra-low friction coefficients, 10 (2009) 1287-1294.

[44] T. Rout, S. Bera, G. Udayabhanu, R. Narayan, Methodologies of Application of Sol-Gel Based Solution onto Substrate: A Review, Journal of Coating Science and Technology, 3 (2016) 9-22.

[45] A.B. Anderson, T.H. Tran, M.J. Hamilton, S.J. Chudzick, B.P. Hastings, M.J. Melchior, R.W. Hergenrother, Platelet deposition and fibrinogen binding on surfaces coated with heparin or friction-reducing polymers, American Journal of Neuroradiology, 17 (1996) 859-863.

[46] T. Yoshioka, K. Tsuru, S. Hayakawa, A. Osaka, Preparation of alginic acid layers on stainless-steel substrates for biomedical applications, Biomaterials, 24 (2003) 2889-2894.

[47] S. Lee, M. Müller, M. Ratoi-Salagean, J. Vörös, S. Pasche, S.M. De Paul, H.A. Spikes, M. Textor, N.D. Spencer, Boundary Lubrication of Oxide Surfaces by Poly(L-lysine)-g-poly(ethylene glycol) (PLL-g-PEG) in Aqueous Media, *Tribology Letters*, 15 (2003) 231-239.

[48] M. Kyomoto, T. Moro, K. Saiga, M. Hashimoto, H. Ito, H. Kawaguchi, Y. Takatori, K. Ishihara, Biomimetic hydration lubrication with various polyelectrolyte layers on cross-linked polyethylene orthopedic bearing materials, *Biomaterials*, 33 (2012) 4451-4459.

[49] R. Ma, R.F. Epan, I. Zhitomirsky, Electrodeposition of hyaluronic acid and hyaluronic acid-bovine serum albumin films from aqueous solutions, *Colloids Surf B Biointerfaces*, 77 (2010) 279-285.

[50] B.P. Purcell, J.A. Elser, A. Mu, K.B. Margulies, J.A. Burdick, Synergistic effects of SDF-1 α chemokine and hyaluronic acid release from degradable hydrogels on directing bone marrow derived cell homing to the myocardium, *Biomaterials*, 33 (2012) 7849-7857.

[51] H.Y. Lee, H.E. Kim, S.H. Jeong, One-pot synthesis of silane-modified hyaluronic acid hydrogels for effective antibacterial drug delivery via sol-gel

stabilization, *Colloids Surf B Biointerfaces*, 174 (2019) 308-315.

[52] A. Singh, M. Corvelli, S.A. Unterman, K.A. Wepasnick, P. McDonnell, J.H. Elisseeff, Enhanced lubrication on tissue and biomaterial surfaces through peptide-mediated binding of hyaluronic acid, *Nat Mater*, 13 (2014) 988-995.

[53] V. Ravi, Siddaramaiah, T.M. Pramod Kumar, Influence of natural polymer coating on novel colon targeting drug delivery system, *J Mater Sci Mater Med*, 19 (2008) 2131-2136.

[54] S. Seuss, A.R. Boccaccini, Electrophoretic deposition of biological macromolecules, drugs, and cells, *Biomacromolecules*, 14 (2013) 3355-3369.

[55] Y. Cheng, X. Luo, J. Betz, G.F. Payne, W.E. Bentley, G.W. Rubloff, Mechanism of anodic electrodeposition of calcium alginate, *Soft Matter*, 7 (2011) 5677.

[56] A. Simchi, F. Pishbin, A.R. Boccaccini, Electrophoretic deposition of chitosan, *Materials Letters*, 63 (2009) 2253-2256.

[57] C. Sanchez, B. Julián, P. Belleville, M. Popall, Applications of hybrid

organic–inorganic nanocomposites, *Journal of Materials Chemistry*, 15 (2005).

[58] C. Sanchez, G.d.A. Soler-Illia, F. Ribot, T. Lalot, C.R. Mayer, V.J.C.o.M. Cabuil, Designed hybrid organic– inorganic nanocomposites from functional nanobuilding blocks, 13 (2001) 3061-3083.

[59] J. Wen, G.L.J.C.o.M. Wilkes, Organic/inorganic hybrid network materials by the sol– gel approach, 8 (1996) 1667-1681.

[60] R. Ma, I. Zhitomirsky, Electrophoretic deposition of silica–hyaluronic acid and titania–hyaluronic acid nanocomposites, *Journal of Alloys and Compounds*, 509 (2011) S510-S513.

[61] O.V. Penkov, M. Khadem, J.S. Lee, M. Kheradmandfard, C.L. Kim, S.W. Cho, D.E. Kim, Highly durable and biocompatible periodical Si/DLC nanocomposite coatings, *Nanoscale*, 10 (2018) 4852-4860.

[62] J. Baek, Y. Fan, S.H. Jeong, H.Y. Lee, H.D. Jung, H.E. Kim, S. Kim, T.S. Jang, Facile strategy involving low-temperature chemical cross-linking to enhance the physical and biological properties of hyaluronic acid hydrogel, *Carbohydr Polym*, 202 (2018) 545-553.

[63] G.J. Owens, R.K. Singh, F. Foroutan, M. Alqaysi, C.-M. Han, C. Mahapatra, H.-W. Kim, J.C. Knowles, Sol–gel based materials for biomedical applications, *Progress in Materials Science*, 77 (2016) 1-79.

[64] F. Sun, I. Zhitomirsky, Electrodeposition of hyaluronic acid and composite films, *Surface Engineering*, 25 (2013) 621-627.

[65] Y. Chen, Y. Ding, J. Zheng, A polymer nanocomposite coating with enhanced hydrophilicity, antibacterial and antibiofouling properties: Role of polymerizable emulsifier/anionic ligand, *Chemical Engineering Journal*, 379 (2020).

[66] R. Bywalez, H. Karacuban, H. Nienhaus, C. Schulz, H.J.N.r.l. Wiggers, Stabilization of mid-sized silicon nanoparticles by functionalization with acrylic acid, 7 (2012) 76.

[67] A. Zhu, A. Cai, Z. Yu, W. Zhou, Film characterization of poly(styrene-butylacrylate-acrylic acid)-silica nanocomposite, *J Colloid Interface Sci*, 322 (2008) 51-58.

- [68] L. Zhai, G. Ling, J. Li, Y. Wang, The effect of nanoparticles on the adhesion of epoxy adhesive, *Materials Letters*, 60 (2006) 3031-3033.
- [69] A. Tutunchi, R. Kamali, A. Kianvash, Adhesive strength of steel–epoxy composite joints bonded with structural acrylic adhesives filled with silica nanoparticles, *Journal of Adhesion Science and Technology*, 29 (2014) 195-206.
- [70] J.H.H. Bongaerts, K. Fourtouni, J.R. Stokes, Soft-tribology: Lubrication in a compliant PDMS–PDMS contact, *Tribology International*, 40 (2007) 1531-1542.
- [71] J. Greenwood, K. Johnson, E.J.W. Matsubara, A surface roughness parameter in Hertz contact, 100 (1984) 47-57.
- [72] R. Guerra Silva, U. Teicher, A. Nestler, A. Brosius, Finite element modeling of chip separation in machining cellular metals, *Advances in Manufacturing*, 3 (2015) 54-62.
- [73] Z. Wang, A.A. Volinsky, N.D. Gallant, Crosslinking effect on polydimethylsiloxane elastic modulus measured by custom-built compression instrument, *Journal of Applied Polymer Science*, 131 (2014) n/a-n/a.

[74] L. Giraud, G. Bazin, S. Giasson, Lubrication with Soft and Hard Two-Dimensional Colloidal Arrays, *Langmuir*, 33 (2017) 3610-3623.

[75] M. Kobayashi, A. Takahara, Tribological properties of hydrophilic polymer brushes under wet conditions, *Chem Rec*, 10 (2010) 208-216.

[76] K. Ishihara, Highly lubricated polymer interfaces for advanced artificial hip joints through biomimetic design, *Polymer Journal*, 47 (2015) 585-597.

[77] Q. Wei, S. Jiang, R. Zhu, X. Wang, S. Wang, Q. Wang, Injectable Peptide Hydrogel Enables Integrated Tandem Enzymes' Superactivity for Cancer Therapy, *iScience*, 14 (2019) 27-35.

[78] C. Dunnill, T. Patton, J. Brennan, J. Barrett, M. Dryden, J. Cooke, D. Leaper, N.T. Georgopoulos, Reactive oxygen species (ROS) and wound healing: the functional role of ROS and emerging ROS-modulating technologies for augmentation of the healing process, *Int Wound J*, 14 (2017) 89-96.

[79] S. Wang, G. Yu, Z. Wang, O. Jacobson, L.S. Lin, W. Yang, H. Deng, Z. He, Y. Liu, Z.Y. Chen, X. Chen, Enhanced Antitumor Efficacy by a Cascade of

Reactive Oxygen Species Generation and Drug Release, *Angew Chem Int Ed Engl*, 58 (2019) 14758-14763.

[80] C. Mao, Y. Xiang, X. Liu, Z. Cui, X. Yang, K.W.K. Yeung, H. Pan, X. Wang, P.K. Chu, S. Wu, Photo-Inspired Antibacterial Activity and Wound Healing Acceleration by Hydrogel Embedded with Ag/Ag@AgCl/ZnO Nanostructures, *ACS Nano*, 11 (2017) 9010-9021.

[81] Y. Wang, Z. Li, Y. Hu, J. Liu, M. Guo, H. Wei, S. Zheng, T. Jiang, X. Sun, Z. Ma, Y. Sun, F. Besenbacher, C. Chen, M. Yu, Photothermal conversion-coordinated Fenton-like and photocatalytic reactions of Cu_{2-x}Se-Au Janus nanoparticles for tri-combination antitumor therapy, *Biomaterials*, 255 (2020) 120167.

[82] P. Sivakumar, M. Lee, Y.-S. Kim, M.S. Shim, Photo-triggered antibacterial and anticancer activities of zinc oxide nanoparticles, *Journal of Materials Chemistry B*, 6 (2018) 4852-4871.

[83] R. Quinones, D. Shoup, G. Behnke, C. Peck, S. Agarwal, R.K. Gupta, J.W. Fagan, K.T. Mueller, R.J. Iuliucci, Q. Wang, Study of Perfluorophosphonic Acid Surface Modifications on Zinc Oxide Nanoparticles, *Materials (Basel)*, 10

(2017).

[84] V. Lakshmi Prasanna, R. Vijayaraghavan, Insight into the Mechanism of Antibacterial Activity of ZnO: Surface Defects Mediated Reactive Oxygen Species Even in the Dark, *Langmuir*, 31 (2015) 9155-9162.

[85] S. Kumar, N.L. Reddy, H.S. Kushwaha, A. Kumar, M.V. Shankar, K. Bhattacharyya, A. Halder, V. Krishnan, Efficient Electron Transfer across a ZnO-MoS₂-Reduced Graphene Oxide Heterojunction for Enhanced Sunlight-Driven Photocatalytic Hydrogen Evolution, *ChemSusChem*, 10 (2017) 3588-3603.

[86] N. Wiesmann, W. Tremel, J. Brieger, Zinc oxide nanoparticles for therapeutic purposes in cancer medicine, *J Mater Chem B*, 8 (2020) 4973-4989.

[87] Y. Zhang, T. R Nayak, H. Hong, W. Cai, Biomedical applications of zinc oxide nanomaterials, *Current molecular medicine*, 13 (2013) 1633-1645.

[88] G. Yi, X. Li, Y. Yuan, Y. Zhang, Redox active Zn/ZnO duo generating superoxide ($\cdot\text{O}_2^-$) and H₂O₂ under all conditions for environmental sanitation, *Environmental Science: Nano*, 6 (2019) 68-74.

- [89] S. Hong, K. Yang, B. Kang, C. Lee, I.T. Song, E. Byun, K.I. Park, S.-W. Cho, H. Lee, Hyaluronic Acid Catechol: A Biopolymer Exhibiting a pH-Dependent Adhesive or Cohesive Property for Human Neural Stem Cell Engineering, *Advanced Functional Materials*, 23 (2013) 1774-1780.
- [90] K.C. Black, Z. Liu, P.B. Messersmith, Catechol Redox Induced Formation of Metal Core-Polymer Shell Nanoparticles, *Chem Mater*, 23 (2011) 1130-1135.
- [91] H.J. Park, Y. Jin, J. Shin, K. Yang, C. Lee, H.S. Yang, S.W. Cho, Catechol-Functionalized Hyaluronic Acid Hydrogels Enhance Angiogenesis and Osteogenesis of Human Adipose-Derived Stem Cells in Critical Tissue Defects, *Biomacromolecules*, 17 (2016) 1939-1948.
- [92] E. Amstad, T. Gillich, I. Bilecka, M. Textor, E. Reimhult, Ultrastable iron oxide nanoparticle colloidal suspensions using dispersants with catechol-derived anchor groups, *Nano letters*, 9 (2009) 4042-4048.
- [93] Q. Li, D.G. Barrett, P.B. Messersmith, N. Holten-Andersen, Controlling Hydrogel Mechanics via Bio-Inspired Polymer-Nanoparticle Bond Dynamics, *ACS Nano*, 10 (2016) 1317-1324.

[94] P. Kord Forooshani, R. Pinnaratip, E. Polega, A.G. Tyo, E. Pearson, B. Liu, T.-O. Folayan, L. Pan, R.M. Rajachar, C.L. Heldt, B.P. Lee, Hydroxyl Radical Generation through the Fenton-like Reaction of Hematin- and Catechol-Functionalized Microgels, *Chemistry of Materials*, 32 (2020) 8182-8194.

[95] J. Yang, M.A. Cohen Stuart, M. Kamperman, Jack of all trades: versatile catechol crosslinking mechanisms, *Chem Soc Rev*, 43 (2014) 8271-8298.

[96] Z. Zhang, X. He, C. Zhou, M. Reaume, M. Wu, B. Liu, B.P. Lee, Iron Magnetic Nanoparticle-Induced ROS Generation from Catechol-Containing Microgel for Environmental and Biomedical Applications, *ACS Appl Mater Interfaces*, 12 (2020) 21210-21220.

[97] X. Lu, S. Shi, H. Li, E. Gerhard, Z. Lu, X. Tan, W. Li, K.M. Rahn, D. Xie, G. Xu, F. Zou, X. Bai, J. Guo, J. Yang, Magnesium oxide-crosslinked low-swelling citrate-based mussel-inspired tissue adhesives, *Biomaterials*, 232 (2020) 119719.

[98] T.I. Kim, B. Kwon, J. Yoon, I.J. Park, G.S. Bang, Y. Park, Y.S. Seo, S.Y. Choi, Antibacterial Activities of Graphene Oxide-Molybdenum Disulfide

Nanocomposite Films, ACS Appl Mater Interfaces, 9 (2017) 7908-7917.

[99] I. Youm, V. Agrahari, J.B. Murowchick, B.B. Youan, Uptake and cytotoxicity of docetaxel-loaded hyaluronic acid-grafted oily core nanocapsules in MDA-MB 231 cancer cells, Pharm Res, 31 (2014) 2439-2452.

[100] A.I. Neto, A.C. Cibrao, C.R. Correia, R.R. Carvalho, G.M. Luz, G.G. Ferrer, G. Botelho, C. Picart, N.M. Alves, J.F. Mano, Nanostructured polymeric coatings based on chitosan and dopamine-modified hyaluronic acid for biomedical applications, Small, 10 (2014) 2459-2469.

[101] A.K. Zak, R. Razali, W.H. Majid, M. Darroudi, Synthesis and characterization of a narrow size distribution of zinc oxide nanoparticles, Int J Nanomedicine, 6 (2011) 1399-1403.

[102] A. Burger, R. Srikantharajah, W. Peukert, A. Hirsch, Individualization and Stabilization of Zinc Oxide Nanorods by Covalent Functionalization with Positively Charged Catechol Derivatives, Chemistry, 23 (2017) 17257-17268.

[103] S.K.S. Parashar, B.S. Murty, S. Repp, S. Weber, E. Erdem, Investigation of intrinsic defects in core-shell structured ZnO nanocrystals, Journal of

Applied Physics, 111 (2012).

[104] T. Rajh, L. Chen, K. Lukas, T. Liu, M. Thurnauer, D. Tiede, Surface restructuring of nanoparticles: an efficient route for ligand– metal oxide crosstalk, *The Journal of Physical Chemistry B*, 106 (2002) 10543-10552.

[105] D. Gan, W. Xing, L. Jiang, J. Fang, C. Zhao, F. Ren, L. Fang, K. Wang, X. Lu, Plant-inspired adhesive and tough hydrogel based on Ag-Lignin nanoparticles-triggered dynamic redox catechol chemistry, *Nat Commun*, 10 (2019) 1487.

[106] Y. Li, J. Wang, Y. Yang, J. Shi, H. Zhang, X. Yao, W. Chen, X. Zhang, A rose bengal/graphene oxide/PVA hybrid hydrogel with enhanced mechanical properties and light-triggered antibacterial activity for wound treatment, *Materials Science and Engineering: C*, 118 (2021).

[107] Z. Song, Y. Wu, H. Wang, H. Han, Synergistic antibacterial effects of curcumin modified silver nanoparticles through ROS-mediated pathways, *Mater Sci Eng C Mater Biol Appl*, 99 (2019) 255-263.

[108] G. Gao, Y.-W. Jiang, H.-R. Jia, F.-G. Wu, Near-infrared light-controllable

on-demand antibiotics release using thermo-sensitive hydrogel-based drug reservoir for combating bacterial infection, *Biomaterials*, 188 (2019) 83-95.

[109] K.Y. Stokes, T.R. Dugas, Y. Tang, H. Garg, E. Guidry, N.S. Bryan, Dietary nitrite prevents hypercholesterolemic microvascular inflammation and reverses endothelial dysfunction, *American Journal of Physiology-Heart and Circulatory Physiology*, 296 (2009) H1281-H1288.

초록 (Abstract)

나노입자를 통해 기능성을 부여한 생체의료용 히알루론산 기반 나노복합체 하이드로젤

서울대학교

재료공학부

황 창 하

가교된 친수성 고분자의 3차원 입체 구조물인 하이드로젤은 현재 훌륭한 생체적합성과 다양한 특성을 변화시킬 수 있는 점은 많은 장점때문에 생체 의료분야에서 각광을 받아왔다. 다양한 고분자들 중에, 우리 몸에 존재하는 생체 다당류인 히알루론산이 훌륭한 생체적합성 때문에 하이드로젤에 토대로서 최근에 많은 연구가 진행되어왔다. 그러나 약한 기계적 물성과 다양한 기능의 부족이 히알루론산의 대표적인 단점으로 지적되어 왔다. 이 연구에서 나노복합체 하이드로젤 시스템이 이러한 단점들을 해결하는 최고의 대안 중 하나로 소개된다. 하이드로젤 구조에서 나노물질의 투입으로 기계적 특성을 향상시킬 뿐만 아니라, 생체 의료 분야에서 요구되는 기능들을 부여 할 수 있다.

첫 번째 연구에서는 전기영동증착법과 솔-겔 방법으로 구

성되는 일련의 과정을 통해 기계적으로 안정하고 유효성이 높은 히알루론산-실리카 나노복합체 코팅을 개발했다. 평균 나노입자의 크기가 약 90 nm인 실리카 나노입자는 히알루론산-실리카 코팅층에 균일하게 분포되어 있고, 나노복합체 코팅층의 두께는 실리카의 함량과 관계없이 약 1-2 μm 인 것을 확인했다. 실리카 나노입자의 투입은 나노복합체 코팅의 기계적 안정성을 증진시키는 역할을 했고, 이는 히알루론산 코팅층과 비교했을 때 더 높은 접착 강도를 갖는다는 것을 의미한다. 또한, 나노복합체 코팅은 훌륭한 생체유효성을 보여주었는데, PDMS 기판을 활용한 맞춤 마찰 실험으로 평가했다. 위 연구로 히알루론산-실리카 나노복합체 코팅은 우수한 생체유효성을 필요로 하는 생체 의료기기에 해결책으로 잠재력을 가지고 있음을 확인했다.

두번째 연구에서는 향상된 항균 치료를 위해 카테콜-산화아연 복합체를 통해 활성산소를 자가 발생시키는 히알루론산 하이드로젤 플랫폼 (HCZ)을 제작하였다. 카테콜-산화아연 복합체가 형성 과정에서 전자의 이동을 통해 활성산소 발생량을 증가시키고, 동시에 히알루론산에 달려있는 카테콜 그룹과 산화아연 나노입자간의 배위결합을 통해 하이드로젤 구조를 제작했다. 이 하이드로젤은 화학적으로 가교 결합한 산화아연 나노입자를 포함한 히알루론산 하이드로젤 (HAZ)과 비교했을 때 기계적 특성 부문에서 다른 양상들을 보여줬다. HCZ 하이드로젤은 HAZ와 비교했을 때 높은 팽윤 비율, 효소에 의한 분해 저항성, 그리고 조직 접합 강도를 나타냈다. 또한, HCZ 하이드로젤로부터 발생하는 증가된 활성산소를 전자스핀 공명법, 과산화수소 농도, 글루타티온 고갈, 세포 내부의 활성산소

측정 등의 방법을 활용해 평가했다. 비록 활성산소가 HCZ 하이드로젤에서 발생하지만, HCZ 10 (10 퍼센트의 산화아연 포함)을 제외한 다른 HCZ 하이드로젤들에서는 독성이 보이지 않았다. 이는 낮은 농도의 산화아연 나노입자는 세포 특성에 미치지 않는다는 것을 의미한다. HCZ 하이드로젤의 향상된 항균 효과도 두가지 박테리아 균에 대해 생체 내, 외에서의 박테리아 실험을 통해 증명되었다. 결론적으로 위 연구는 많은 양의 활성산소를 발생시키는 카테콜-산화아연 복합체를 통해 제작된 하이드로젤의 항균 치료용으로서의 가능성을 증명하였다.

종합해보면 이 연구들은 히알루론산 하이드로젤에 다양한 나노입자가 들어감으로서 기계적 물성을 증진시키고 생체 의료분야에서 필요로 하는 추가적인 기능을 할당할 수 있다는 것을 증명할 수 있었다. 실리카 나노입자의 투입으로 기존보다 증가된 기계적 안정성과 생체 순환성을 확보할 수 있었다. 게다가, 카테콜-산화아연 배위 결합 복합체로부터 증가된 활성산소를 통해 향상된 항균 효과도 확보 할 수 있었다.

주요어: 하이드로젤; 히알루론산; 나노복합체 하이드로젤; 실리카 나노입자; 생체순환성; 산화아연 나노입자; 카테콜; 활성산소; 항균 특성

학번: 2017-21069

감사의 글 (Acknowledgement)

2017년 봄, 처음 대학원에 진학해 연구실에 들어와 선배들에게 인사할 때가 생생하게 기억나는데 벌써 졸업을 앞두고 있다는 사실에 감회가 새롭습니다. 길다면 길고, 짧다면 짧은 시간동안 많은 일들이 있었습니다. 대학원에 다니는 동안 많은 분들에게 연구적인 부분 뿐만 아니라 정서적, 인격적인 부분에서도 긍정적인 영향을 많이 받았습니다. 아무것도 모르던 채로 대학원에 입학한 제가 박사 학위를 취득한 것은 주변에 있었던 많은 분들 덕분이라 생각되고, 감사인사를 짧게나마 이렇게 글로 남기려고 합니다.

먼저 저의 인생에 대해 항상 아낌없이 응원해주고 지지해주는 부모님과 동생에게 진심으로 감사의 말씀을 전하고 싶습니다. 대학원 과정동안 기쁜일도 있었고, 힘든일도 있었지만 그 때마다 아낌없는 조언을 주시고 항상 저의 결정을 지지해 주셨기에 제가 더욱더 흔들림없이 대학원을 다닐 수 있는 원동력이 되었습니다. 하루는 친구같이, 다른 하루는 멘토처럼 조언해주시는 게 이번 기회를 빌어 항상 사랑하고 감사한다는 말씀을 전하고 싶습니다. 앞으로는 저도 부모님께 든든한 버팀목처럼 힘이 될 수 있도록 최선을 다하겠습니다. 그리고 동생한테는 대학원에 다니면서 잘 챙겨주지 못한 거 같아서 마음이 쓰이네. 이직하는 곳에서의 생활도 잘 하면 좋겠고, 이후에 또 다른 도전을 하게된다면 적극적으로 응원할게.

그리고 저의 지도 교수님인 김현이 교수님께도 감사의 인사를 드리고 싶습니다. 2013년, 제가 학부 2학년 때 교수님 수업인

재료역학 개론을 수강했었습니다. 그 당시에 교수님께서 상담을 하고 싶은 학생은 언제든지 찾아오라고 하셨고, 저는 교수님을 찾아뵙어서 대학원 진학에 대한 고민상담을 했었습니다. 그 때 했던 상담으로 인해 저는 대학원 진학을 결심했었고, 이 후에 교수님 밑에서 지도를 받은걸로 봤을 때 학교를 다니는 동안 교수님께 정말로 많은 도움을 받았다는 것을 새삼 느끼게 됩니다. 그리고 대학원에 다니는 도중에도 저에게 아낌없는 조언을 해주신 것들이 생각이 나고 앞으로의 여정에서도 실천할 수 있도록 항상 노력하겠습니다. 교수님의 제자였었기에 제가 한걸음 더 성장해서 사회로 나갈 수 있는 것 같습니다. 항상 존경하고 감사드립니다.

또한, 저의 박사 학위 논문 심사를 맡아주셨던 안철희 교수님, 선정운 교수님, 한철민 교수님, 정현도 교수님께도 감사의 인사를 드립니다. 저의 부족한 부분에 대해 아낌없이 조언해 주신 덕분에 저의 박사 학위 논문이 좀 더 발전했다고 생각합니다. 교수님들의 조언을 바탕으로 앞으로의 연구 과정에서도 적용시키며 발전하도록 노력하겠습니다. 정말 감사드립니다.

긴 시간동안 가장 많이 만났을 BMA 멤버들에게도 감사의 말씀을 남깁니다. 연구 과제를 주도하며 진행해주시고, 항상 적극적으로 조언을 해주신 이성미 박사님에게 감사 인사를 드립니다. 아무것도 몰랐던 때부터 조언을 아끼지 않아주셔서 대학원에 진학했을 때보다는 좀 더 발전된 상태로 졸업할 수 있게 되는 것 같습니다. 저에게 해주셨던 조언들을 바탕으로 앞으로 더욱더 성숙되고 발전된 모습으로 지내겠습니다. 저의 대학원 생활에서 가장 큰 도움을 주셨던 설하 누나에게도 감사의 인사를 남깁니다. 저의 첫 논문과

마지막 논문의 교신저자를 맡아 주시고 많은 토론을 통해 논문을 완성시키는 과정이 정말로 인상깊었습니다. 그리고 항상 새로운 방향으로 연구를 발전시키는 모습을 보면서 대학원 생활 내내 연구적인 부분에서 많은 귀감을 얻었습니다. 육아와 연구를 병행하는 모습을 보면서도 항상 대단하다고 생각을 했고, 저도 그런 모습을 본받아서 매순간 최선을 다해야 겠다고 생각했습니다. 앞으로 누나의 앞길에도 좋은 일만 가득하기를 언제나 응원하고 있겠습니다. 논문 지도를 열심히 해주신 한철민 교수님께도 감사의 인사를 드립니다. 거리가 먼 데도 불구하고 서울에 자주 오셔서 아낌없이 조언을 해주시던 모습을 잊지 않겠습니다. 항상 편안하게 저를 대해주신 것 같아 좀 더 수월하게 논문 작업을 할 수 있었던 것 같습니다. 처음 연구실에 왔을 때 커피를 사주시며 조언을 해주시던 장태식 박사님, 그 조언이 저의 초기 연구실 생활에 방향성을 잡아줬어서 정말 감사하게 생각합니다. 이 후에도 세미나에서 적극적으로 디스커션을 해주셔서 저의 연구에도 큰 발전이 있던 것 같습니다. 마지막 연구 주제에서 동물실험 부분을 도와주신 박지웅 교수님에게도 감사인사를 드립니다. 동물실험 관련해 많은 조언을 얻고 그 결과 논문의 질적 향상을 이끌어 낼 수 있었던 것 같습니다. 또한 과제 관련해 실험을 진행하며 도움을 주셨던 안민경 박사님에게도 감사의 인사를 드립니다.

연구실의 든든한 맏형이었던 현이형, 항상 일을 잘하고 후배들과 거리낌없이 어울리면서도 술선수범하는 모습이 인상 깊었습니다. 형에게 맨 처음 배운 피피티 제작방법은 아마 평생 사용하지 않을까 싶습니다 ㅎㅎ 그 이외에도 일하는 법과 연구에서의 조언들을

평생 간직하며 지내겠습니다 감사합니다. 비슷하게 히알루론산 연구를 한 호용이형, 연구에 관해서 영감을 많이 받았었고 히알루론산을 다룬다는 점에서 묘하게 동질감을 많이 느꼈었습니다. 항상 활기찼던 모습으로 기억나는 다영누나, 같은 하이드로젤 피플이라 도움도 많이 받았던거 같아서 감사합니다. 그리고 누나가 여러가지 운동들이나 새로운 것에 시도하는 모습이 인상적이었어요. 광희형은 저한테 있어서 일을 잘하고 열심히 하는 이미지였어요. 물론 그 때문에 항상 힘들어하셨지만... 항상 친절하고 일에 대해서도 잘 알려주셔서 정말 감사했습니다. 윤정누나랑은 진영이형과 같이 서핑갔던 때가 가장 기억에 남네요. 항상 살갑게 해주셔서 저도 연구실 생활을 맘 편히 할 수 있었던거 같아요. 천일이형이랑은 갑작스럽게 과제에 참여하게 되었을 때 많이 도움을 받았던게 생각이 나요. 그 때는 정말 막막한 심정이었는데 형이 있었어서 좀 더 빠르게 익숙해진거 같아서 감사했습니다. 은호형은 짧은 시간에 많은 논문을 쓰는 것을 봤을 때 굉장히 본받고 싶다고 생각했어요. 저랑 낮잠 듀오로 같이 연구실에서 잤던 기억이 새록새록 나네요. 인구형이랑은 같이 와인 먹으면서 더 친해진 것 같아서 좋았어요. 항상 편안하게 도와줘서 고맙고 앞으로도 와인 모임하면서 자주 뵙시다! 경일이형과는 많이 대화를 나누지는 못했지만 연구적으로 많은 도움을 주셔서 감사했어요. 석우형이랑은 카페 103 메이트였는데 형이 졸업하고나서 거의 가질 않았네요. 연구실에서 잘 해주셔서 재밌는 연구실 생활했던거 같아요. 지금은 미국으로 가서 연구하는 민규, 혼자서 미국 가서 연구하는 모습을 봤을 때 정말 대단하다고 생각했어. 이렇게 스스로 찾아서 연구하는 모습도 놀라웠고, 연구자의 꿈이 확고한거

에서도 굉장히 대단하다고 생각했어. 같이 산자부 과제 미팅 갔을 때 너가 레크리에이션 준비해온게 아직도 생각나네. 산자부 과제가 하면서 그래도 많이 친해진거 같아. 앞으로도 연구 파이팅하고 성과도 잘 나오기를 바랄게.

같이 마지막으로 연구실을 정리하는 진영이형과 수형이에게도 감사의 말을 남깁니다. 진영이형은 정말 사람을 편하게 해주는 능력이 있는거 같아요. 말도 잘통하고 친절해서 저랑 더욱 친해질 수 있었던 거 같아요. 서핑갔던 것과 최근에 여수 같이 간 것 등등 많은 일들을 같이 했던 게 새록새록 생각나네요. 앞으로도 원하는 일 다 잘됐으면 좋겠습니다. 수형이와는 이제 10년지기 친구인데 학부 다닐때만 해도 이렇게 오래 같이 볼지 예상치 못했네. 그래도 같이 들어온 게 너였어서 좀 더 편하고 의지하면서 연구실 생활을 잘 할 수 있었던거 같아. 너가 일을 잘 처리하는 모습 보면서 왜 그렇게 해야하는데 라고 생각했던 적이 많았던거 같다 ㅎㅎ 앞으로도 회사가서도 같이 파이팅하자.

또한 대학원 생활하면서 저와 같이 시간을 보내며 행복하게 해주었던 히스 친구들, 같이 춤췄던 그루비 코드, 솔라팸, 서울 리퍼 친구들, 과동기들 에게도 모두 감사의 인사를 드립니다. 그리고 사랑하는 여자친구 소민이에게도 곁에 있어줘서 고맙다고 전해주고 싶습니다. 다시 한번 제가 박사 학위를 받을 수 있게 도와주신 많은 분들께 감사인사를 드리고, 앞으로 저도 연구자로서 새로운 분야에서도 발전하는 모습을 보여드리겠습니다.